Photooxygenation in an advanced led-driven flow reactor module: Experimental investigations and modelling

Robbie Radjagobalou, Jean-François Blanco, Odile Dechy-Cabaret, M. Oelgemoller, Karine Loubiere

Photooxygenation in an advanced led-driven flow reactor module: Experimental investigations and modelling

Robbie Radjagobalou[a,b], Jean-François Blanco[a], Odile Dechy-Cabaret[b], Michael Oelgemöller[c], Karine Loubière[a,*]

[a] Laboratoire de Génie Chimique LGC, Université de Toulouse, CNRS, Toulouse, France
[b] Laboratoire de Chimie de Coordination LCC, CNRS, Toulouse, France
[c] James Cook University, College of Science and Engineering, Townsville, Queensland 4811, Australia

A B S T R A C T

The photooxygenation of α-terpinene was investigated as a benchmark reaction in an advanced LED-driven flow reactor module, both from an experimental and modelling point of view. Ethanol was used as a green solvent and rose Bengal was chosen as a cheap sensitizer of industrial importance. Firstly, the kinetic law based on all mechanistic steps was established for the chosen photooxygenation. From this, the set of operating parameters potentially influencing the photoreaction rate were identified. Subsequently, experiments were carried out under continuous-flow conditions to screen these operating parameters, namely concentration of α-terpinene, concentration of photosensitizer, residence time, structure of the segmented gas-liquid flow and nature of the reagent gas phase (air *versus* pure oxygen). Finally, the conditions enabling minimization of sensitizer bleaching were established. It was also shown that the hydrodynamic characteristics of the gas-liquid flow can have an effect on the conversion levels. From this, a simplified model was proposed to predict the conversion at the reactor's outlet when pure oxygen was used.

1. Introduction

The growth of the chemical industry during the 21st century has put pressure on the availability of raw materials. Traditional manufacturing processes of chemicals have thus been evaluated and reviewed according to the principles of Green Chemistry and Green Engineering [1,2]. As part of this changed manufacturing philosophy, photochemistry has emerged as a key synthesis pathway and technology for sustainable chemistry [3–5]. Photochemical reactions have significantly enriched the organic synthesis portfolio as it allows for the rapid construction of complex molecules using photons as a traceless reagent [6,7]. As a consequence, photochemical processes are currently becoming widespread [8], in particular in the search of new biologically active compounds for applications in medicine or agriculture, as well as in many other fields (healthcare, material and environmental sciences for instance) [9–11].

Among the established photochemical transformations, dye-sensitized photooxygenations involving singlet oxygen $^1O_2$ are particularly attractive [12–14] (*i. e.* photooxygenations of terpenes or the synthesis of the antimalarial drug artemisinin). $^1O_2$ is generated by photosensitization of triplet molecular oxygen $^3O_2$, most often in the visible range with catalytic amounts of an organic sensitizer (dye). When compared to chemical pathways, the photooxidation route avoids the use of strong, hazardous or persistent oxidants and leads to highly selective oxygenations. Despite these advantages, these photochemical reactions have generally not found widespread implementations in the chemical industry, mainly due to the specific reaction conditions (large dilution and/or poor light penetration) and the use of specialized equipment and energy-demanding mercury lamps (intensive cooling, limited lifetime). Continuous-flow (microstructured) technologies have recently emerged as alternatives to batch processing and their suitability for photooxygenation reactions has been demonstrated [15–23]. The combination of these devices with LED light sources additionally offers promising solutions for improving operation safety and controlling the emitted light spectrum, thus enabling energy-savings while at the same time increasing yields and selectivity [24,25].

At present, there are few studies to understand and predict the performances of photooxygenations in a chemical engineering context [26–28]. In most cases, the kinetic law associated with this rather complex photochemical reaction is not rigorously established, in particular considering the full reactional mechanism. The possible occurrence of mixing and/or gas-liquid mass transfer limitations and their

Nomenclature

A_{520}	Absorbance at 520 nm (−)
d_{pen}	Characteristic light penetration distance (m)
d_c	Diameter of the tube (m)
d^*	Ratio between d_{pen} and d_c (−)
D	Coefficient of diffusion ($m^2\,s^{-1}$)
E	Spherical irradiance ($mol\,m^{-2}\,s^{-1}$)
e^a_{RB}	Volumetric rate of photon absorption of rose Bengal ($mol\,m^{-3}\,s$)
F_{O2}	Inlet molar flowrate of oxygen ($mol\,s^{-1}$)
$F_{RB,MAX}$	Maximal molar flowrate of rose Bengal ($mol\,s^{-1}$)
$F_{\alpha T}$	Inlet molar flowrate of α-terpinene ($mol\,s^{-1}$)
f	Inlet stoichiometric ratio (−)
k_R	Kinetic constant associated with the formation of ascaridole ($L\,mol^{-1}\,s^{-1}$)
k_d	Kinetic constant associated with the whole deactivation pathways of $^1O_2$ (s^{-1})
L_b	Length of bubbles (m)
L_s	Length of liquid slugs (m)
Q_G	Inlet volumetric gas flowrate ($m^3\,s^{-1}$)
Q_L	Inlet volumetric liquid flowrate ($m^3\,s^{-1}$)
q	Inlet volumetric ratio (−)
q_e	Photon flux emitted by the light source ($mol\,s^{-1}$)
q_p	Incident photon flux received in the reactor ($mol\,s^{-1}$)
MM	Molar mass ($kg\,mol^{-1}$)
r	Local molar volumetric reaction rate ($mol\,m^{-3}\,s^{-1}$)
STY_j	Space Time Yield relative to the experiment j (−)
V_{film}	Volume of liquid film (m^3)
V_L	Volume of liquid in the reactor (m^3)
V_{LS}	Volume of a liquid slug (m^3)
V_R	Volume of reactor (m^3)

Greek letters

$\chi_{\alpha T}$	Conversion in α-terpinene (%)
χ_{RB}	Rate of photobleaching (%)
ε_G	Gas retention in the reactor (−)
φ^1O_2	Quantum yield of singlet oxygen formation in ethanol by rose Bengal (−)
ϕ_T	Overall quantum efficiency of the photooxygenation (−)
$\phi_{^1RB^* \rightarrow {}^3RB^*}$	Efficiency of the formation of triplet $^3RB^*$ from the singlet state $^1RB^*$ (−)
$\phi^0_{^3RB^* \rightarrow {}^1O_2}$	Efficiency of the singlet oxygen formation from triplet $^3RB^*$ without the quenching by α-terpinene (−)
$\phi_{^3RB^* \rightarrow {}^1O_2}$	Efficiency of the formation of singlet oxygen from the triplet state $^3RB^*$ (−)
$\phi_{^1O_2 \rightarrow Asc}$	Efficiency of the formation of ascaridole from singlet oxygen addition (−)
κ	Naperian molar absorption coefficient ($m^2\,mol^{-1}$)
$\bar{\kappa}$	Naperian molar absorption coefficient in the case of a polychromatic light source ($m^2\,mol^{-1}$)
$\bar{\kappa}_a$	Naperian molar absorption coefficient in the case of a polychromatic light source calculated with the method a ($m^2\,mol^{-1}$)
$\bar{\kappa}_b$	Naperian molar absorption coefficient in the case of a polychromatic light source calculated with the method b ($m^2\,mol^{-1}$)
ϑ	Ratio of the factor of response relative to a gas chromatography analysis (−)
λ	Wavelength (m)
θ	Dilution rate applied to determine the absorbance at 520 nm (−)
ρ_G	Density of the gas ($kg\,m^{-3}$)
τ	Residence time (s)
τ_i	Irradiation time (s)
τ_R	Characteristic time of the photooxygenation reaction (s)
τ_{diff}	Characteristic time of diffusion (s)
τ_{conv}	Characteristic time of convection (s)

Dimensionless number

φ_C	Competition between the photobleaching of rose Bengal by α-terpinene and the formation of singlet oxygen from the triplet state $^3RB^*$ (−)
φ_{O_2}	Competition between the formation of singlet oxygen and the photobleaching of rose Bengal (−)
φ_{RB}	Competition between the physical deactivation processes and the photobleaching of the triplet state $^3RB^*$ (−)
Ca	Capillary's number (−)
Da_I	Damköhler I number (−)

Molecule

αT	α-Terpinene
Asc	Ascaridole
pC	p-Cymene
RB	Rose Bengal

Subscript

ET	Energy transfer
Flu	Fluorescence
IC	Internal conversion
ISC	Intersystem crossing
Oct	Relative to 1-octene
Ph	Phosphorescence
0	Initial value (*i. e.* τ = 0 s)
1	Relative to the volume of the reactor equal to 5 mL
2	Relative to the volume of the reactor equal to 2 mL

Superscript

β	Apparent order relative to α-terpinene in the kinetic equation of the photobleaching (Eq. (12))
γ	Apparent order relative to α-terpinene in the kinetic equation of the reaction between singlet oxygen and α-terpinene (Eq. (5))

effect on the photochemical reaction rate are also rarely studied and quantified. This obvious research gap might be partly due to a lack of modelling tools for the coupling of transport phenomena (including gas-liquid mass transfer), reaction kinetics and transport of light (radiative transfer). A multidisciplinary approach is thus needed to address the challenges of photochemical engineering. In previous studies [29–32], advanced models, validated by tailored experiments, were proposed to predict the performances of simple homogeneous photochemical reactions in LED-driven microreactors. A set of equations describing the phenomena controlling the reaction outputs (conversion, photonic efficiency) was established and numerically solved considering a 2D geometry. This approach included radiative transfer (two-flux model) and mass transport equations (laminar flow), coupled *via* a photochemical kinetic term. It was demonstrated, on the one hand, that mass transfer limitations exist even in microreactors, and that they can lead to a decrease in conversion and, on the other hand, that a methodology can be established to define which operating conditions (reaction channel diameter/depth, photon flux and residence time) should

be chosen to overcome these limitations.

In keeping with this context, this study aimed at investigating, based on modelling approaches and dedicated experiments in an advanced flow reactor, how and why the operating conditions (hydrodynamic conditions, initial concentration of reagents *etc.*) can affect the performances of a sensitized photooxygenation. The underlying objective was to illustrate that some of the current issues with the implementation of heterogeneous two-phase photochemical reactions under flow conditions can be addressed using a chemical engineering framework [32]. Such a framework is indeed essential to develop a process intensification strategy, which enables adaptation of the continuous-flow photoreactor design and of the operating domain to photochemical reaction characteristics, and more generally a transfer from batch to continuous mode operations. For that, a benchmark photoreaction was chosen and studied using an advanced LED-driven flow reactor module. In the first part, the reaction system investigated (*i. e.* the photooxygenation of α-terpinene in ethanol with rose Bengal as photosensitizer) was analysed and the kinetic law associated with the photooxygenation of α-terpinene rigorously established. The analysis of the kinetic law expression was then used as a means to provide an experimental strategy to identify the key operating parameters. In a second part, the photoreactor and light source used (*i. e.* the Vapourtec® easy-photochem E-series) were described and the experimental protocol for monitoring the reaction established. Then, preliminary experiments were conducted to investigate the photobleaching ability of rose Bengal. From this, various sets of experiments were carried out to study the effect of the operating conditions previously identified. Subsequently, the coupling between the various phenomena was highlighted and an operating window identified to conveniently conduct the photoreaction. Finally, the first simplified model to describe the dependancy of the conversion with residence times when pure oxygen is used was developed.

2. Background & kinetic law

This section will first describe the reactional system that has been chosen for this study, namely the sensitized photooxygenation of α-terpinene using ethanol as solvent and rose Bengal as sensitizer. Secondly, the kinetic law associated with this reaction will be established based on mechanistic considerations. From this, the potentially critical steps will be discussed, enabling to choose the relevant experiments to be carried out in order to study how and why the operating conditions (hydrodynamics conditions, initial concentration of reagents *etc.*) can affect the performances of the sensitized photooxygenation.

2.1. Description of the reactional system investigated

The reactional system chosen is the photooxygenation of α-terpinene to ascaridole, illustrated in Fig. 1. This photoreaction has been widely studied in batch reactors, and some examples have been realized in microreactors [33–38]. Ascaridole was historically used as an anthelmintic and was recently found to show antimalarial activity [39]. The reaction is frequently chosen as a benchmark photoreaction, in particular to evaluate the performances of new photosensitizers (soluble or solid-supported) or new operating conditions [40,41].

The main product of the photooxygenation is ascaridole, a stable endoperoxide at 25 °C and 1 atm, formed *via* [4 + 2] cycloaddition of singlet oxygen to the diene. p-Cymene is commonly obtained as a minor product [40]. Several pathways responsible for the formation of p-cymene have been discussed.

In the present study, a green solvent, ethanol, was chosen even though the lifetime of singlet oxygen is significantly lower in this solvent than in chlorinated solvents (160–265 μs in chloroform *versus* 13.5 μs in ethanol [13]). Air was used as a safe supply of oxygen. The photosensitizer employed was rose Bengal (RB), which offers several advantages: transition metal-free, non-toxic, cheap, of industrial importance [42], soluble in polar-protic solvents and possessing intense absorption bands in the visible range, and especially in the region between 450 nm and 600 nm. RB absorbs strongly around 550 nm and generates singlet oxygen with a high quantum yield ($\phi^{1}O_2 \approx 0.75$ in ethanol [43]). The main drawback of RB is its strong ability to degrade. Indeed, it is well-known that RB involved in a photochemical system is sensitive to light exposure and/or subject to (side) reactions, thus causing a discoloration of the reaction mixture, commonly referred to as photobleaching. When occurring, the solution does no longer contain sufficient RB for the desired photosensitized reaction to operate and instead, the autooxidation of α-terpinene into p-cymene becomes dominant [40]. For this reason, using RB in ethanol as photosensitizer is sometimes considered as non-efficient, in particular in batch reactors. In a kinetic study, the photochemical pathways leading to the photobleaching of RB cannot be neglected as it naturally leads to a decrease in ascaridole formation. In practice, a rigorous monitoring of the stability of RB must be implemented to avoid or minimize photobleaching.

2.2. Establishment of the overall kinetic law

The pathways associated with the formation of the photo-excited species and with their deactivation (fluorescence, phosphorescence, intersystem crossing and internal conversion) will be assumed as elementary steps [43–45]; the kinetic rate associated to excited species will then follow a first-order law.

2.2.1. Main pathway (formation of ascaridole)

First, rose Bengal (RB) is photo-excited by absorption of photons in the visible range (480–600 nm) (Eq. (1)).

$$1^{st}\text{step}: \ RB \xrightarrow{h\nu} {}^{1}RB^{*} \quad \text{with} \quad r_{Abs} = e^{a}_{RB} \tag{1}$$

It is important to note that this is the sole photochemical step in the entire mechanism of the photooxygenation. Its reaction rate is directly proportional to the volumetric rate of photon absorption of rose Bengal, e^{a}_{RB}, that is the number of photons absorbed by RB per unit of time and per unit of liquid volume. This spectral and local quantity depends on the naperian linear absorption coefficient of the species RB, noted α_{RB} (m^{-1}), and on the spherical irradiance E (mol $m^{-2} s^{-1}$), according to

$$e^{a}_{RB} = \alpha_{RB}.\ E = \kappa_{RB}.\ [RB].E \tag{2}$$

Where κ_{RB} (m^2 mol^{-1}) is the naperian α_{RB} molar absorption coefficient of RB and [RB] (mol m^{-3}) C_{RB} the concentration of RB.

The *second step* corresponds to the formation of the triplet excited rose Bengal $^{3}RB^{*}$ from the singlet state $^{1}RB^{*}$ through intersystem crossing (ISC) (Eq. (3)). Subsequently, energy transfer (ET) between the triplet $^{3}RB^{*}$ and the ground state of oxygen $^{3}O_2$ [*third step*] leads to the formation of the singlet oxygen $^{1}O_2$ (Eq. (4)). Finally, singlet oxygen

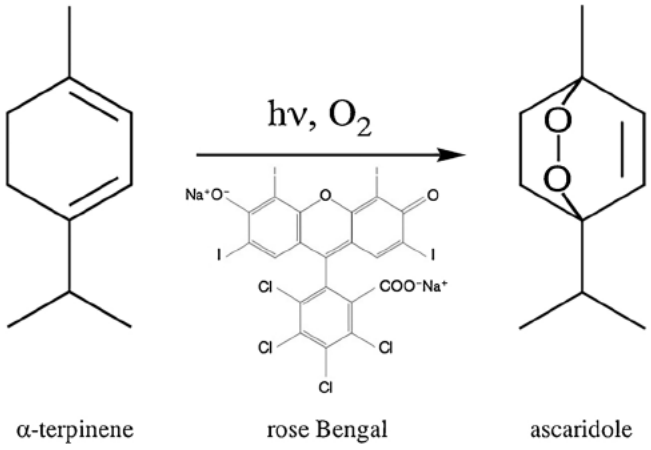

Fig. 1. Photooxygenation of α-terpinene.

reacts thermally with α-terpinene (αT) to form ascaridole (Asc) (Eq. (5)) [*fourth step*]. For the purpose of standardization, an order γ (> 0) for αT was chosen for the last step as, at present, no publication has dealt with a rigorous determination of this order.

$$2^{nd}\text{step}: {}^1RB^* \rightarrow {}^3RB^* \quad \text{with} \quad r_{ISC}^{^1RB} = k_{ISC}^{^1RB}.[{}^1RB^*] \tag{3}$$

$$3^{rd}\text{step}: {}^3RB^* + O_2 \rightarrow RB + {}^1O_2 \quad \text{with} \quad r_{O2} = k_{ET}.[{}^3RB^*][O_2] \tag{4}$$

$$4^{th}\text{step}: {}^1O_2 + \alpha T \rightarrow Asc \quad \text{with} \quad r_R = k_R.[{}^1O_2][\alpha T]^\gamma \tag{5}$$

2.2.2. Pathways for the deactivation of photoexcited rose Bengal

Once generated, $^1RB^*$ can be either deactivated by fluorescence (Eq. (6)) or by internal conversion (IC) (Eq. (7)) and $^3RB^*$ either by phosphorescence (Eq. (8)) or by internal conversion (Eq. (9)). $^3RB^*$ can also be quenched by the solvent (here ethanol) in the reaction medium (Eq. (10)).

$$^1RB^* \rightarrow RB + h\nu \quad \text{with} \quad r_{flu}^{^1RB} = k_{flu}^{^1RB}.[{}^1RB^*] \tag{6}$$

$$^1RB^* \rightarrow RB \quad \text{with} \quad r_{IC}^{^1RB} = k_{IC}^{^1RB}.[{}^1RB^*] \tag{7}$$

$$^3RB^* \rightarrow RB + h\nu \quad \text{with} \quad r_{Ph}^{^3RB} = k_{Ph}^{^3RB}.[{}^3RB^*] \tag{8}$$

$$^3RB^* \rightarrow RB \quad \text{with} \quad r_{IC}^{^3RB} = k_{IC}^{^3RB}.[{}^3RB^*] \tag{9}$$

$$^3RB^* + EtOH \rightarrow RB + EtOH \quad \text{with} \quad r_{EtOH}^{^3RB} = k_{EtOH}^{^3RB}.[{}^3RB^*][EtOH] \tag{10}$$

2.2.3. Pathways for the photobleaching of rose Bengal

Two types of mechanisms can lead to an irreversible transformation of RB from its triplet state, thus changing its light absorption properties and subsequently reducing its efficiency as a photosensitizer. This process corresponds to the so-called photobleaching of rose Bengal.

An electron transfer from $^3RB^*$ to the ground state of oxygen $^3O_2$ (Eq. (11)) can produce the corresponding radical ion $RB^{\bullet-}$, superoxide $^{\bullet-}O_2$, or various other radical species [46]. This reaction is thermodynamically favourable. Alternatively, a reaction between $^3RB^*$ and α-terpinene by hydrogen transfer can occur leading to the formation of p-cymene and a polycyclic molecule, schematically noted RB_{H2} (Eq. (12)) [46–48]. In both pathways, the structure of RB changes and the resulting molecules ($^{\bullet-}O_2$ and RB_{H2}) have different chemical properties and subsequently fates.

$$^3RB^* + O_2 \rightarrow RB^{\bullet-} + {}^{\bullet-}O_2 \quad r_{O_2}^{^3RB} = k_{O_2}^{^3RB}.[RB^{3*}][O_2] \tag{11}$$

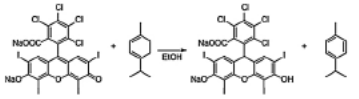

$$r_P = k_P.[{}^3RB^*][\alpha T]^\beta \tag{12}$$

Here also, an order β > 0 for α-terpinene has been inserted by default.

2.2.4. Pathways for the deactivation of singlet oxygen by photophysical processes

Singlet oxygen, $^1O_2$, may be deactivated by internal conversion (Eq. (13)) or fluorescence (Eq. (14)). $^1O_2$ can also be deactivated to molecular oxygen by the solvent (Eq. (15)).

$$^1O_2 \rightarrow O_2 \quad r_{IC}^{O_2} = k_{IC}^{O_2}.[{}^1O_2] \tag{13}$$

$$^1O_2 \rightarrow O_2 + h\nu \quad r_{flu}^{O_2} = k_{flu}^{O_2}.[{}^1O_2]. \tag{14}$$

$$^1O_2 + EtOH \rightarrow O_2 + EtOH \quad r_{EtOH}^{O_2} = k_{EtOH}^{O_2}.[{}^1O_2][EtOH] \tag{15}$$

From the elementary steps previously described, the overall kinetic rate associated with the sensitized photooxygenation of α-terpinene, namely the overall consumption rate of α-terpinene by the reactions, noted r, can be established. It is expressed as Eq. (16),

$$r = r_R + r_P = k_R.[{}^1O_2][\alpha T]^\gamma + k_P.[{}^3RB^*][\alpha T]^\beta \tag{16}$$

Where r_R is the consumption rate of α-terpinene by the main pathway (*i. e.* the one leading to the formation of ascaridole, see Section 2.2.1.) and r_P is the consumption rate of α-terpinene resulting from its interaction with the photoexcited $^3RB^*$ (side-reaction).

It is important to consider that the lifetimes of intermediate photoexcited species are in the order of nano- to milliseconds. Therefore, the steady state assumption can be reasonably applied to $^1RB^*$, $^3RB^*$ and $^1O_2$ (Eq. (17)), leading to

$$\frac{d[{}^1RB^*]}{dt} \approx \frac{d[{}^3RB^*]}{dt} \approx \frac{d[{}^1O_2]}{dt} \approx 0 \tag{17}$$

One can then show that the concentrations of $^1RB^*$, $^3RB^*$ and $^1O_2$, respectively, are expressed as

$$[{}^1RB^*] = \frac{e_{RB}^a}{k_{flu}^{^1RB} + k_{IC}^{^1RB} + k_{ISC}^{^1RB}} \tag{18}$$

$$[{}^3RB^*] = \frac{k_{ISC}^{^1RB}.[{}^1RB^*]}{k_{Ph}^{^3RB} + k_{IC}^{^3RB} + k_{EtOH}^{^3RB}.[EtOH] + k_P.[\alpha T]^\beta + k_{O_2}^{^3RB}.[O_2] + k_{ET}.[O_2]} \tag{19}$$

$$[{}^1O_2] = \frac{k_{ET}.[O_2][{}^3RB^*]}{k_{flu}^{O_2} + k_{IC}^{O_2} + k_{EtOH}^{O_2}.[EtOH] + k_R.[\alpha T]^\gamma} \tag{20}$$

The overall kinetic constant $k_Q^{RB^3}$ related to the photobleaching of RB can be defined as

$$k_Q^{^3RB} = k_P.[\alpha T]^\beta + k_{O_2}^{^3RB}.[O_2] \tag{21}$$

By combining Eqs. (19), (20) and (21) with Eqs. (16) and (17), one can obtain that

$$r = k_R.[\alpha T]^\gamma. \left[\frac{k_{ET}.[O_2]}{k_{flu}^{O_2} + k_{IC}^{O_2} + k_{EtOH}^{O_2}.[EtOH] + k_R.[\alpha T]^\gamma}\right] \left[\frac{k_{ISC}^{^1RB}}{k_{Ph}^{^3RB} + k_{IC}^{^3RB} + k_{EtOH}^{^3RB}.[EtOH] + k_Q^{^3RB} + k_{ET}.[O_2]}\right] \left[\frac{e_{RB}^a}{k_{flu}^{^1RB} + k_{IC}^{^1RB} + k_{ISC}^{^1RB}}\right] + k_P.[\alpha T]^\beta. \left[\frac{k_{ISC}^{^1RB}}{k_{Ph}^{^3RB} + k_{IC}^{^3RB} + k_{EtOH}^{^3RB}.[EtOH] + k_Q^{^3RB} + k_{ET}.[O_2]}\right] \left[\frac{e_{RB}^a}{k_{flu}^{^1RB} + k_{IC}^{^1RB} + k_{ISC}^{^1RB}}\right] \tag{22}$$

Which can be written as

$$r = e_{RB}^a.\phi_T \tag{23}$$

Where ϕ_T is the overall quantum efficiency of the photooxygenation defined by

$$\phi_T = \left(\phi_{^1RB^* \rightarrow {}^3RB^*}\right).\left(\phi_{^3RB^* \rightarrow {}^1O_2}\right).\left(\phi_{^1O_2 \rightarrow Asc} + \varphi_C\right) \tag{24}$$

With,

- e_{RB}^a (mol m^{-3} s^{-1}) is the volumetric rate of photon absorption previously defined in Eq. (2).
- $\phi_{^1RB^* \rightarrow {}^3RB^*}$ is the efficiency of the formation of triplet $^3RB^*$ from the

singlet state $^1RB^*$, and is defined by Eq. (25). This dimensionless number evaluates the efficiency of the *second step*. If the intersystem crossing process is predominant with respect to the different deactivation processes of the singlet state $^1RB^*$, then $\phi^1_{RB^*} \rightarrow {}^3_{RB^*} \approx 1$.

$$\phi_{^1RB^* \rightarrow {}^3RB^*} = \frac{k^{1RB}_{ISC}}{k^{1RB}_{flu} + k^{1RB}_{IC} + k^{1RB}_{ISC}} \quad (25)$$

- $\phi^3_{RB^*} \rightarrow {}^1_{O_2}$ is the efficiency for the formation of $^1O_2$ from the triplet state $^3RB^*$, defined by Eq. (26). This dimensionless number evaluates the efficiency of the *third step*. If the transfer of energy between $^3RB^*$ and O_2 is the predominant pathway with respect to the different processes responsible for the deactivation and/or quenching of the triplet state $^3RB^*$, then $\phi^3_{RB^*} \rightarrow {}^1_{O_2} \approx 1$.

$$\phi_{^3RB^* \rightarrow {}^1O_2} = \frac{k_{ET}.\,[O_2]}{k^{3RB}_{Ph} + k^{3RB}_{IC} + k^{3RB}_{EtOH}.\,[EtOH] + k^{3RB}_{Q} + k_{ET}.\,[O_2]} \quad (26)$$

- $\phi^1_{O_2} \rightarrow {}_{Asc}$ is the efficiency for the formation of ascaridole from $^1O_2$ addition, defined by Eq. (27). This dimensionless number evaluates the efficiency of the *fourth step*. If the chemical reaction of α-terpinene with singlet oxygen is faster than the deactivation of singlet oxygen, then $\phi^1_{O_2} \rightarrow {}_{Asc} \approx 1$.

$$\phi_{^1O_2 \rightarrow Asc} = \frac{k_R.\,[\alpha T]^\gamma}{k^{O_2}_{flu} + k^{O_2}_{IC} + k^{O_2}_{EtOH}.\,[EtOH] + k_R.\,[\alpha T]^\gamma} \quad (27)$$

- The ratio φ_C represents the competition between the photobleaching of RB by α-terpinene and the formation of singlet oxygen from the triplet state $^3RB^*$, according to

$$\varphi_C = \frac{k_P.\,[\alpha T]^\beta}{k_{ET}.\,[O_2]} \quad (28)$$

Therefore, it is clearly linked to the *third step*.

Thus, by using dimensionless numbers, the expression of the overall kinetic law (Eq. (23)) enables to describe and formalize the different routes involved in the photooxygenation.

2.3. Theoretical discussion on the parameters driving the critical steps of the photooxygenation

Based on Eq. (23), it is interesting to discuss the contribution of each parameter to the overall kinetic law of the photooxygenation reaction in order to identify the possible critical step(s) of the global reaction and thus to define which specific experiments are required to validate these assumptions.

Firstly, it is commonly assumed that the triplet state $^3RB^*$ is more stable than the singlet state $^1RB^*$ since the triplet state has a much longer lifetime [49]. Thus, the intersystem crossing, *i. e.* the *second step* Eq. (3), occurs spontaneously and quickly in the reaction media. Besides, the reactivity of $^1O_2$ is known to be very high in the presence of a diene component like α-terpinene since $^1O_2$ is electrophilic [*fourth step*]. As a result, the kinetic constant of the reaction between singlet oxygen and α-terpinene, noted k_R, is assumed to be significantly higher than the overall kinetic constant, noted k_d, associated with the deactivation of singlet oxygen (Eq. (29)). This leads to

$$k_R.\,[\alpha T]^\gamma > k_d = k^{O_2}_{Flu} + k^{O_2}_{IC} + k^{O_2}_{EtOH}.\,[EtOH] \quad (29)$$

The values of k_R and k_d were experimentally determined by assuming $\gamma = 1$ and were approximately equal to 10^7 L mol^{-1} s^{-1} [50] and 10^4 s^{-1} [44], respectively. From these one can deduce the minimal initial concentration of α-terpinene, noted $[\alpha T]_{0,MIN}$, to fullfill the condition of Eq. (29). Therefore Eq. (29) is valid if, and only if, $[\alpha T]_0 \geq [\alpha T]_{0,MIN} = 0.001$ mol L^{-1} in the case of $\gamma = 1$.

As a consequence, the efficiencies characterizing the *second step* and the *fourth step*, $\phi^1_{RB^*} \rightarrow {}^3_{RB^*}$ and $\phi^1_{O_2} \rightarrow {}_{Asc}$ are very likely high (> 0.7). Then, the two remaining critical steps are the absorption of a photon by RB (*first step*) and the formation of $^1O_2$ (*third step*), which mainly control the overall reaction rate r. Subsequently, a deeper analysis of the expression of the volumetric rate of photon absorption, e^a_{RB}, and of the yield of singlet oxygen formation, $\phi^3_{RB^*} \rightarrow {}^1O_2$, is required to identify the experimental key parameters for selective ascaridole formation.

As shown in Eq. (2), e^a_{RB} depends on the concentration fields of species (which could be affected by the hydrodynamic conditions, namely the mixing in the liquid phase and the gas-liquid mass transfer), but also on the absorption properties of the medium and on the irradiance fields. This relationship clearly shows how, when implementing a photochemical reaction, the radiative transfer equation (RTE), which enables to predict the field of irradiance E, is strongly coupled with other conservation equations *via* this physical quantity e^a_{RB}. As explained by [32], adding this new coupling significantly increases the degree of complexity of the modelling approach, all the more that the radiative transfer equation is intrinsically complex. Whatever the methods used to solve RTE (*i. e.* analytical or numerical ones), one should remember that e^a_{RB} mainly depends on (i) the incident photon flux density (q_p) that can be precisely measured by chemical actinometry [29,51,52] and on (ii) the optical properties of the reaction medium.

In the studied photochemical system, no scattering by the reaction medium exists (absence of particles) and the only absorbing specie in the visible range of radiation is the photosensitizer, RB, implying thus that the absorbance of the reaction medium will remain constant (*i. e.* be independent from the conversion level) if no photobleaching exists.

Another important issue is that due to the exponential attenuation of light, some gradients of concentration inevitably exist inside the reactional medium and that they can be accentuated by the hydrodynamics conditions (for example a poor mixing). These physical limitations can significantly slow down the photochemical reaction rate and decrease the performances of the process (productivity, photonic efficiency) [31]. To identify these limitations, and thus to elaborate a strategy to overcome or to minimize them, specific experiments should be carried out as well as modelling.

When carrying out sensitized photooxygenations in continuous-flow microreactors, in particular under Taylor flow conditions, the contact between the various reactive species (*i. e.* the frequencies of reactive collisions) will be mainly controlled by the mixing in the liquid slugs between two consecutives bubbles and in the liquid film close to the walls. As a consequence, one can expect that the structure of the gas-liquid flow (for example the occurrence of short or long bubbles) can influence the performances at the outlet of the microreactor. At present, little attention has been paid to this question in the literature, although several studies related to the implementation of sensitized photooxygenations in microreactors have been performed.

The other critical step is the generation of singlet oxygen $^1O_2$ (*the third step*). Its efficiency is expressed by Eq. (26) which can be written again as follows so as to highlight new relevant dimensionless numbers;

$$\phi_{^3RB^* \rightarrow {}^1O_2} = \frac{\varphi_{O_2}}{1 + \varphi_{O_2} + {}_{RB}} \quad (30)$$

With

$$\varphi_{O_2} = \frac{k_{ET}.\,[O_2]}{k^{3RB}_{Q}} \quad (31)$$

$$\varphi_{RB} = \frac{k^{3RB}_{Ph} + k^{3RB}_{IC} + k^{3RB}_{EtOH}.\,[EtOH]}{k^{3RB}_{Q}} \quad (32)$$

The ratio φ_{O2} represents the competition between the formation of $^1O_2$ and the photobleaching of RB. If $\varphi_{O2} > > 1$, then $^1O_2$ is

predominantly formed while the case where $\varphi_{O2} << 1$ the photobleaching of RB (*i. e.* a discoloration of the solution) occurs. From Eq. (31), one can observe that high concentration of dissolved oxygen tends to favour the formation of singlet oxygen.

The ratio φ_{RB} represents the competition between the physical deactivation processes and the photobleaching of the triplet state $^3RB^*$. In other words, φ_{RB} measures the fastest pathway to produce unreactive photoexcited rose Bengal. If $\varphi_{RB} >> 1$, then RB is physically deactivated to its ground state and thus potentially reusable as a photosensitizer. In contrast, if $\varphi_{RB} << 1$, then the molecular structure of RB will change into RB_{H2} (see Eq. (12)) and the moles of RB in the medium will decrease leading to a discoloration. Following the variation of the solution's absorbance is a simple method to identify the predominant processes.

Introducing these two dimensionless numbers enables to indicate that the limiting pathway in the *third step* should be the photobleaching of RB. This implies that one should find operating conditions leading to $\varphi_{O2} > \varphi_{RB} >> 1$, that is the ones that limit or avoid the photobleaching pathway.

3. Material & methods

3.1. Light source and reactor

The E-Series UV-150 photochemical reactor designed and constructed by Vapourtec® was chosen as a convenient continuous-flow device to implement the photooxygenation of α-terpinene. Due to its design and the way of operating the device, a broad and rapid screening of the operating parameters was made possible. The reactor's capillary itself was a tube made of fluorinated ethylene propylene and with an inner diameter equal to 1.3 mm and a wall thickness of 0.15 mm. Different lengths were available, thus enabling different reactor volumes of 2 mL, 5 mL or 10 mL, respectively. As shown in Fig. 2, the reactor has a coiled capillary design where the tube was fixed to a solid cartridge, with the lamp inserted at its centre.

As the photooxygenation required radiation between 450 nm and 600 nm (according to the spectral absorption domain of RB, see Fig. 3, the light source chosen was a LED array composed of two types of LEDs

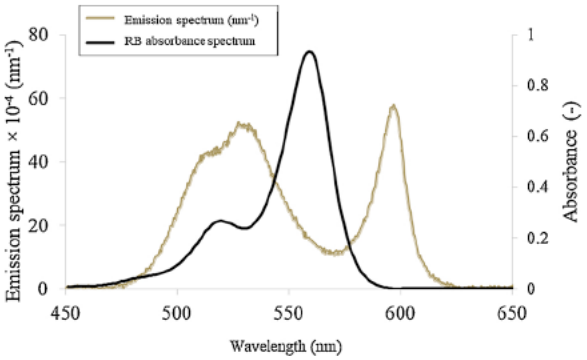

Fig. 3. Example of the absorbance spectrum of RB ([RB] = 9.5×10^{-6} mol L^{-1}) and emission spectrum of the LED array used in the E-Series UV-150 photochemical reactor.

(4 LEDs emitting at 530 nm and 2 LEDs emitting at 580 nm). The radiant power emitted, noted q_e, was equal to 3.8 W (technical data) corresponding to a photon flux q_e close to 1.7×10^{-5} mol s^{-1} (see Supplementary material, Section 1). The emission spectrum of the LED array is represented in Fig. 3.

The temperature of the reactive medium was measured at the outer surface of the tube using a sensor and was equal to 28 °C for all experiments. The E-Series platform was equipped with three high performance V-3 peristaltic pumps with a maximum flow rate of 10 mL min^{-1} each. Air or pure oxygen were used; their flow rates were controlled using an ALICAT Scientific MC-10 SCCM (DISM, SIN, GAS Air) mass flow controller. Air was supplied from a Charles Austen pump Dymax 30. A T-junction with an internal diameter of 1 mm was used to supply gas bubbles to the liquid flow. All experiments were performed in the Taylor flow regime, which consisted of a series of reproducible and regular liquid slugs and bubbles (Fig. 4. In this regime, the bubbles adopt a characteristic semi-hemispheric shape and nearly completely filled the channel cross-section where a thin liquid film separated them from the channel wall. Such gas-liquid flows offer the advantages of being perfectly structured, easily tuneable (*i. e.* by simply changing both liquid and gas flow rates and/or their ratios) and stable

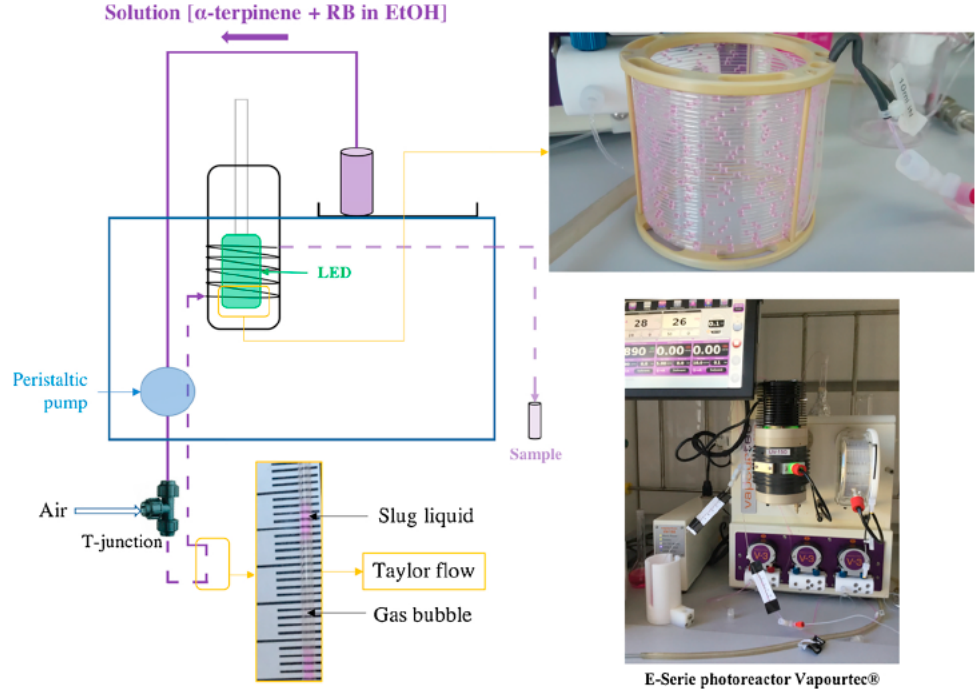

Fig. 2. Image and schematic representation of the E-Series Photoreactor by Vapourtec® and the experimental protocol.

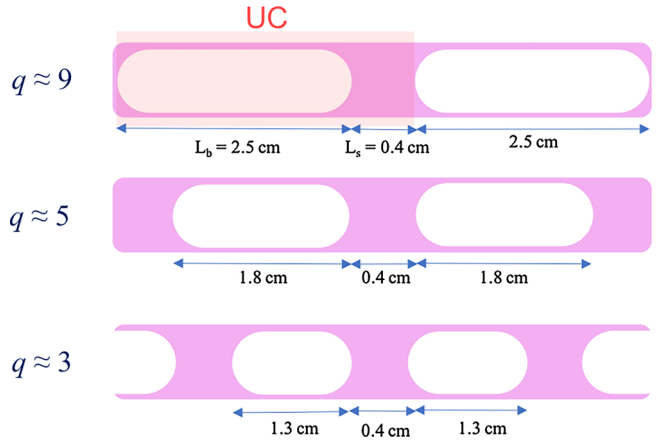

Fig. 4. Schematic representation of the Taylor flow configurations used in the experiments, depending on the ratio of volumetric flow rates q. The lengths are given with a standard deviation of 0.1 cm. A Unit Cell, noticed UC, is composed of one bubble and one liquid slug.

[59,60,62]. For all experiments, the latter characteristics were verified as the length of the reactor coil was not too long (the effect of pressure drop was negligible) and the mass transfer between gas and liquid phases was insignificant (a notable decrease of the bubble size did not occur along the tubing length).

The reaction mixture was collected at the outlet *via* the waste/collection switching valve in an amber glass vial. A schematic representation of the device and an image illustrating the Taylor flow are presented in Fig. 2. For all the experiments, the lengths of the gas bubbles (L_b) and the liquid slugs (L_s) were systematically measured using a camera at the inlet and the outlet of reactor.

As mentioned above, all experiments were carried out under Taylor flow conditions. For that, preliminary studies were performed to identify the operating domain leading to this type of segmented flow. It was observed that the spatial repartition of gas and liquid phases inside the tube was mainly driven by the volumetric ratio, noted q, between the volumetric air flowrate Q_G and the volumetric liquid flowrate Q_L (Eq. (33)).

$$q = \frac{Q_G}{Q_L} \tag{33}$$

The different configurations studied in this work are reported in Fig. 4. From the desired residence time τ and q, the values of Q_G and Q_L were deduced (see Supplementary material, Section 2).

The molar flow rate of O_2, noted F_{O2} (mol s^{-1}), that can be delivered by each bubble, is another key parameter. It can be estimated from Q_G (Eq. (34)).

$$F_{O_2} = \left(\frac{\%[O_2].\,\rho_G}{MM_G}\right).\,Q_G = \left(\frac{\%[O_2].P}{R.\,T}\right).\,Q_G \tag{34}$$

Where ρ_G (in kg m^{-3}) is the density of the gas at the operating pressure/temperature, MM_G (in kg.mol^{-1}) the molar mass of air, $\%[O_2]$ the percentage of oxygen in the gas, T the operating temperature and P the operating pressure.

In addition, the stoichiometric proportion of the different reactants at the entrance of the microreactor was determined by the stoichiometric ratio, noted f, defined as the ratio between the inlet molar flow rate of O_2 and of α-terpinene (Eq. (35)); $f > 1$ corresponds to an excess of oxygen and $f < 1$ to a default of oxygen, while the stoichiometric condition is reached for $f = 1$.

$$f = \frac{F_{O_2}}{F_{\alpha T}} \tag{35}$$

Finally, the initial concentration of α-terpinene, noted $[\alpha T]_0$, was deduced from the values of q and f as shown in Eq. (36).

$$[\alpha T]_0 = \frac{F_{\alpha T}}{Q_L} = \frac{F_{O_2}}{f.\,Q_L} = \left(\frac{\%[O_2].P}{R.\,T}\right).\,\frac{q}{f} \tag{36}$$

The irradiation time, noted τ_i, of the reaction medium was equal to the residence time in the tube section exposed to light (the tube section between the T-junction and the entry in the irradiated chamber being not taken into account). This was calculated as the ratio between the volume of reactor V_R and the total inlet volume flow rate Q_T ($= Q_G + Q_L$). It should be noted that such a calculation is an estimation. Due to the presence of a liquid film surrounding each bubble, the bubbles move faster than the sum of both gas and liquid superficial velocities, inducing the occurrence of a slipping velocity. The bubble velocity can be determined by image acquisition and analysis [58] or by solving numerically the mass and momentum conservations for the heterogeneous gas-liquid system [59–63] From them, the exact residence time τ could be deduced.

3.2. General procedure for the photooxygenation of α-terpinene

Rose Bengal sodium salt (CAS: 11121-48-5; purity ≥ 94%; 1017 g mol^{-1}; Sigma–Aldrich), α-terpinene (CAS: 99-86-6; purity ≥ 89%; 136.17 g mol^{-1}; Sigma–Aldrich), p-cymene (CAS: 99-87-6; purity ≥ 97%; 134.22 g mol^{-1}; Sigma–Aldrich) were used in solution with ethanol (CAS: 64-17-5; purity = 96%; 46.07 g mol^{-1}; Merck). Ascaridole (CAS: 512-85-6; purity ≈ 93%; 168.23 g mol^{-1}) was previously isolated by vacuum distillation in the group of M. Oelgemöller. The commercial α-terpinene from Sigma-Aldrich contained two main impurities: p-cymene (2% in mass) and eucalyptol (CAS: 470-82-6; 154.25 g mol^{-1}, 8% in mass), as well as other minor unidentified species (1% in mass).

The reaction medium was prepared by dissolving a mass of RB in a 100 mL volumetric flask wrapped in aluminium foil containing ethanol (3×10^{-5} mol L^{-1} < $[RB]_0$ < 7×10^{-5} mol L^{-1}). Then, a mass of α-terpinene was added to the solution (0.03 mol L^{-1} < $[\alpha T]_0$ < 0.15 mol L^{-1}) in a way that the specification of the value of f targeted (lack of O_2, stoichiometric proportion or excess of O_2) was respected. The volumetric flask was also covered at the top with aluminium foil.

In the Vapourtec® reactor module, the reaction medium entered the coiled reactor from the bottom as illustrated in Fig. 2. In this configuration, the effect of gravitational acceleration was decreased leading to a higher stability of the gas-liquid flow in the range of flow rates tested. The reaction medium was pumped by a V-3 peristaltic pump and exposed to light for a duration equal to three times the residence time so as to ensure a steady state. Subsequently, several analytical protocols were applied to measure (i) the photobleaching rate, (ii) the conversion rate and to evaluate (iii) the purity of ascaridole formed.

All product solutions were analysed on the same day to minimize the effect of ambient light. All the experiments were carried out at a temperature of 28 °C and a pressure of 1.1 bar.

3.3. Analytical protocols

Ultraviolet-Visible (UV–vis) absorption spectra of the reaction media were measured at 25 °C on a Shimadzu UV-1800 instrument in a quartz cell of 1 cm (length) in the dark (software UVProbe, step of 1 nm, range of 200–700 nm).

Gas Chromatographic (GC) analysis was performed on an Agilent 7890 gas chromatograph using the Agilent OpenLAB Control Panel and 7683B auto-injector with a controlled method (carrier gas: He, 24 psi; injector: T = 150 °C; split ratio = 25:1; oven program: 50°C (1 min) – 230 °C (1 min) at 25 °C min^{-1}; FID detector (300 °C, gas makeup N_2 at 25 mL.min^{-1}); injection volume = 1 µL). The column used was a Phenomenex Zebron ZB-5 low polarity (0.25 mm ID × 0.25 µm film thickness × 25 m length).

Nuclear Magnetic Resonance (NMR) spectra were recorded on a

Bruker Avance 400 spectrometer (^{1}H, 400.15 MHz; zg30 pulse program; NS = 16; D_1 = 1 s) in $CDCl_3$ at 25 °C.

3.3.1. Monitoring of the photobleaching of RB

The photobleaching level, noted χ_{RB}, was measured by UV–vis spectrophotometry for each operating condition. It represents the percentage of RB photobleached with respect to the initial amount and is defined as

$$\chi_{RB} = 1 - \frac{[RB]}{[RB]_0} \tag{37}$$

UV–vis spectra were recorded immediately after collection as prolonged exposure to air allowed for partial regeneration of RB, as noticeable from a colour intensification. The variation of the absorbance of the reaction media was followed at 520 nm since the other species, αT, pC and Asc, did not absorb in the visible range. Subsequently, the absorbance at 520 nm, noted A_{520}, was proportional to the concentration of RB;

$$A_{520} = l.\ \varepsilon^{RB}_{520}.\ [RB] \tag{38}$$

Where l is the distance of light penetration (1 cm in the quartz cell) and ε^{RB}_{520} is the molar absorption coefficient of RB, $\varepsilon^{RB}_{520} = 3.09 \times 10^4$ L mol^{-1} cm^{-1} (see Supplementary material, Section 3).

3.3.2. Monitoring of the conversion of α-terpinene

The conversion of αT was defined according to

$$\chi_{\alpha T} = 1 - \frac{[\alpha T]}{[\alpha T]_0} \tag{39}$$

The concentration in α-terpinene at the reactor's outlet was followed according to the procedure described by Ronzani et al. [40], either by UV–vis spectrophotometry or by GC analysis.

a) UV–vis measurements

The conversion in αT was determined by following the medium absorbance at 265 nm, taking into account the contribution of each species as follows;

$$\chi_{\alpha T} = \frac{1}{(\varepsilon^{Asc}_{265} - \varepsilon^{\alpha T}_{265}).\ [\alpha T]_0}.\left(\frac{\theta}{l}.\ A_{265}(\tau) - \varepsilon^{pC}_{265}.\left(\frac{p_{pC}}{p_T}\right)\left(\frac{MM_{\alpha T}}{MM_{pC}}\right).\ [\alpha T]_0 - \varepsilon^{RB}_{265}.\ (1 - \chi_{RB}(\tau)).\ [RB]_0 - \varepsilon^{\alpha T}_{265}.\ [\alpha T]_0\right) \tag{40}$$

Where θ is the dilution level applied to the solution to determine A_{265}. $MM_{\alpha T}$ and MM_{pC} are the molar mass of αT and of pC, respectively. The different molar absorption coefficients at 265 nm are detailed in the Supplementary material, Section 3.

b) GC measurements

1-Octene (CAS: 111-66-0; analytical standard (99.9%); 112.21 g mol^{-1}; Sigma–Aldrich) was used as internal standard in all GC measurements. Calibration curves of αT, pC and Asc were prepared in the range of concentrations used in the study (See Supplementary material, Section 4). All the prepared solutions for the calibrations were stored in the fridge and covered with aluminium foil. The retention time of 1-octene, αT, pC and Asc were equal to 2.49 min, 4.35 min, 4.41 min and 5.99 min, respectively. The areas of αT, pC and Asc were determined with 3%, 3.5%, and 1.5% of residual standard deviation, respectively.

The conversion in αT was determined by Eq. (41).

$$\chi_{\alpha T} = 1 - \frac{1}{[\alpha T]_0.\ V_E}.\left(\frac{1}{MM_{\alpha T}.\ V_E}.\ \frac{S_{\alpha T}.\ [Oct]_0.\ V_{Oct}}{S_{Oct}.\ \vartheta_{\alpha T}}\right) \tag{41}$$

Where V_E is the injected volume to the vial (for the analysis) of the reaction medium, $[Oct]_0$ the concentration of the standard 1-octene solution, V_{Oct} the injected volume to the vial of the standard 1-octene solution, $S_{\alpha T}$ the area of αT peak from the chromatogram, S_{Oct} the area of 1-octene peak from the chromatogram and $\vartheta_{\alpha T}$ the ratio factor of response of αT from the calibration curve.

3.3.3. Determination of yield of ascaridole

The methodology implemented consisted in determining the conversion in αT and then the percentage of by-products formed by GC. This enabled to evaluate if the conversion level, $\chi_{\alpha T}$, was equal or not to the yield in ascaridole, noted ρ_{Asc}, defined as the ratio between the moles of Asc formed and the initial moles of αT.

For all the experiments, it was observed that the reaction media contained ascaridole, p-cymene, eucalyptol (4.47 min), α-terpinene (if $\chi_{\alpha T} < 99\%$) and other non-identified components (> 6 min, see Supplementary material, Figure SM.10). Eucalyptol originated from the initial solution of αT did not react with light (subsequently its peak area did not change during the reaction). Therefore, eucalyptol was considered as an unreactive species (and could be used as an internal standard to monitor the conversion rate). The formation of iso-ascaridole was avoided by adjusting the injection temperature to 150 °C [40]. According to Eq. (12), p-cymene can be formed in negligible molar quantities as $[\alpha T]_0 > > [RB]_0 \approx 10^{-5}$ mol L^{-1}. Furthermore, the other non-identified components were the initial impurities of the commercial αT solution according to their retention time. Thus, for all the experiments conducted in the Vapourtec® reactor module, it was shown that the conversion rate of α-terpinene, $\chi_{\alpha T}$, corresponded reasonably well to ρ_{Asc}.

4. Results & discussion

4.1. Preliminary experiments: photobleaching of RB

As a preliminary step, four experiments were carried out under continuous-flow conditions in visible light using the LED-driven Vapourtec® reactor to better understand the photobleaching ability of rose Bengal. The results are shown in Table 1. The temperature recorded at the surface of the tube was equal to 28 °C when the LED light source was switched on. The total input volume flow rate delivered at the entrance of the reactor Q_T was equal to 2.38 mL min^{-1}, the ratio between the gas and liquid volumetric flow rates, *q*, was 5, the ratio of O_2 and αT molar flow rates, *f*, was 1.7 and the reactor volume, V_R, was 5 mL.

In *Entry a*, a typical set of initial conditions leading to a quantitative conversion with a high level of photobleaching (> 50%) is presented. In *Entry b*, a solution of RB dissolved in ethanol containing Asc (and without αT) was prepared to evaluate the effect of quenching by Asc. In *Entry c*, a solution of RB dissolved in ethanol (without αT) was prepared to investigate the effect of quenching by O_2. In *Entry d*, a Taylor flow structure was established with a solution of RB dissolved in ethanol containing αT and argon gas, in order to study the effect of quenching by αT.

Entry c shows that O_2 does not participate significantly in the

Table 1
Experiments conducted in the Vapourtec® reactor to evaluate the photobleaching pathway. q ≈ 5.

Entry	τ (s)	$[\alpha T]_0$ (mol L^{-1})	$[RB]_0$ ($\times 10^{-5}$ mol L^{-1})	$[Asc]_0$ (mol L^{-1})	*f*	χ_{RB} (τ) (%)	$\chi_{\alpha T}$ (τ) (%)
a	126	0.036	4.20	0	1.7	73	99
b	126	0	4.34	0.030	2.1	7	–
c	126	0	4.06	0	–	3	–
d	126	0.037	5.08	0	–	82	–

photobleaching of RB. Comparing *Entry b* with *Entry c*, it can be concluded that, even if the presence of ascaridole increases slightly χ_{RB} from 3% to 7%, ascaridole is not responsible for the substantial photobleaching previously observed. In addition, according to *Entry a* (corresponding to the photooxygenation conditions), the conversion level is nearly quantitative. This means that at least at the outlet of the microreactor, the concentration in ascaridole is equal to 0.036 mol L^{-1} and yet, the photobleaching rate of RB is high (73%) while in *Entry b*, the photobleaching rate is low (7%) for an equivalent concentration of 0.030 mol L^{-1} of ascaridole. Thus, the quenching by ascaridole and O_2 are not the dominant pathways. Finally, *Entry d* confirms the dominant role of αT in the mechanism of photobleaching of RB. The photobleaching rate is equal to 82% in the absence of O_2 and is thus in the same order as the one observed under the photooxygenation conditions (*Entry a*).

Table 2 shows an additional experiment (*Entry e*) where the reaction media is prepared in a 100 mL volumetric flask and hidden from light with agitation for almost 2 h. The result obtained allowed to conclude that RB is stable in a solution containing EtOH, αT and pre-dissolved O_2 in the dark. Consequently, the photobleaching of RB would occur exclusively in the presence of visible light, namely when photoexcited species are generated.

Based on these preliminary experiments, the expression of the overall kinetic constant of the photobleaching of RB, $k_Q^{RB^3}$, defined in Eq. (21), can be simplified to

$$k_Q^{RB^3} \approx k_P.\ [\alpha T]^{\beta} \tag{42}$$

The dimensionless number ϕ_{O2} defined in Eq. (31), was then simplified too;

$$\varphi_{O_2} \approx \frac{k_{ET}.\ [O_2]}{k_P.\ [\alpha T]^{\beta}} \tag{43}$$

By combining Eqs. (23), (24), (28) and (43) the kinetic law can be rewritten in the form of a basic product between a quantum yield and a volumetric rate of photon absorption, as encountered for elementary photochemical reactions.

$$r \approx e^{a}_{RB}.\ \phi_{^1RB^* \rightarrow {}^3RB^*} \left(\frac{1}{1 + \frac{1}{\varphi_{O_2}} + \frac{\varphi_{RB}}{\varphi_{O_2}}} \right) \left(\phi_{^1O_2 \rightarrow Asc} + \frac{1}{\varphi_{O_2}} \right) \tag{44}$$

Eq. (44) clearly shows that the increase of the photochemical reaction rate requires to look for the operating conditions which lead to a rise of φ_{O2}, that is to favour the formation of singlet oxygen rather than the photobleaching reaction. This requirement can be achieved, on the one hand, by increasing the concentration of dissolved oxygen (for example by increasing the pressure or by using pure oxygen) or/and by decreasing the concentration of αT in the liquid phase. As the latter option is not advisable for productivity purposes, maximizing the dissolved oxygen concentration remains the best solution to favour selectivity towards ascaridole. On the other hand, the ratio φ_{O2} can be increased by increasing the collision frequency between $^3RB^*$ and O_2, since the kinetic constants k_{ET} is dependent on the energy state and size of molecules, and thus on the physical properties of the reaction medium and on the Brownian motion of molecules. As a result, experimental operating conditions combining efficient mixing, fast gas-liquid mass transfer and excess of oxygen should be implemented to favour the production of ascaridole.

This preliminary study enabled to simplify the expression of the overall kinetic law according to (Eq. 44). The objectives of the next experiments were to vigorously investigate the influence of each parameter (residence time, concentration of reactants, hydrodynamic conditions) and their coupled influence on the production of ascaridole.

4.2. Effect of residence time

Fig. 5 presents the variation of the conversion of αT and the photobleaching level with residence time (the experiments were conducted with a reactor volume, V_R, equal to 5 mL). In order to study separately the effect of the residence time, the volumetric flow rate ratio q and the stoichiometric parameter f were kept constant for all the experiments ($q \approx 5$ and $f \approx 1.7$); for that, both liquid and gas flow rates were increased in the same proportion. It was firstly observed that quantitative conversion was obtained within 100 s and that αT was selectively converted into ascaridole (no impurities were detected by GC, except the ones initially present in the starting material). Independent of the residence time, the photobleaching level was maintained below 50%. Therefore, ascaridole is obtained with excellent selectivity in about one minute without significantly degrading the photosensitizer. The Space Time Yield, noted STY, can be introduced (as defined in Supplementary material, Section 5) to estimate the productivity of ascaridole per unit of volume. For the best operating condition {τ = 85 s; $\chi_{\alpha T}$ = 99%}, the corresponding Space Time Yield, noted STY_{AIR}, was equal to 4.3×10^{-4} mol s^{-1} L^{-1} (or 5.9×10^{-2} g s^{-1} L^{-1}). It was found in the same order of those obtained in previous studies [38], $STY_1 = 9.4 \times 10^{-4}$ mol s^{-1} L^{-1}; [64], $STY_2 = 8.9 \times 10^{-3}$ mol s^{-1} L^{-1}; [22], $STY_3 = 6.9 \times 10^{-4}$ mol s^{-1} L^{-1}.

Another important conclusion deduced from Fig. 5 is that photobleaching and photooxygenation coexisted in the reaction media. This shows that under these specific operating conditions, the number of absorbed photons, the initial concentration of RB, the mixing and gas-liquid mass transfer characteristics favour the photooxygenation pathway. *A fortiori*, this demonstrates that an operating domain (concentration, flow rate, light power) can be identified that allows a quantitative and selective conversion to ascaridole although the photobleaching is operating. This constitutes an important and promising result, in particular from an industrial perspective that aims at implementing, in meso-scale continuous-flow microstructured equipment, sensitized photooxygenations under green conditions (ethanol) and with a low-cost photosensitizer (RB). The photobleaching of RB becomes less problematic as operating conditions enabling its control can be identified.

The increase of the photobleaching level with the residence time observed in Fig. 5 can be explained by the combination of two phenomena:

1. The frequency of collisions between RB and αT increases with increasing the residence time; hence the interaction probability between these two compounds increases, therefore the kinetic constant k_p associated with the quenching reaction by αT increases.
2. The total volumetric flow rate Q_T controls the residence time. The decrease of the residence time implies an increase of Q_T, and as the reactor volume remains identical as well as q and f, the averaged velocity of both phases, and consequently their fields, increase too. Therefore, the mixing efficiency in the liquid phase (in particular in the liquid slugs characterized by the occurrence of two recirculation loops), the contact time between gas and liquid phases, and subsequently, the overall liquid-side mass transfer coefficient K_L are enhanced. For experiments with small residence times, the amount of dissolved oxygen in the liquid phase is thus probably higher, favouring the photooxygenation pathway with respect to the photobleaching one, which is in accordance with the established model (see Eq. (44)).

Table 2
Experiment under dark condition.

Entry	f	$[\alpha T]_0$ (mol L^{-1})	$[RB]_0$ (mol L^{-1})	V (mL)	χ_{RB} (%)
e	2.2	0.099	4.40×10^{-5}	100	0.73

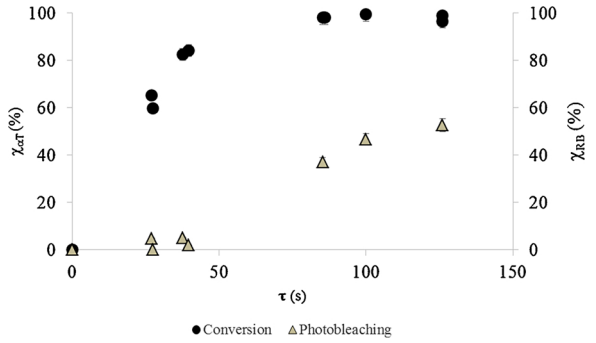

Fig. 5. Variation of the conversion of αT $\chi_{\alpha T}$ (%) and the photobleaching level χ_{RB} (%) with the residence time for V_R = 5 mL, a volumetric flow rate ratio q ≈ 5 and an excess of oxygen f ≈ 1.7. $[\alpha T]_0 = 0.037\ mol\ L^{-1}$ and $[RB]_0 = 4.0 \times 10^{-5}\ mol\ L^{-1}$.

4.3. Effect of the medium absorbance

According to the expression of the kinetic law (Eq. (44)), a variation of the concentration in RB should impact on the conversion rate since the volumetric rate of photon absorption e^a_{RB} depends on this parameter. Indeed, the higher the concentration of RB in the medium, the stronger the medium absorbance will be. Consequently, for a given incident photon flux density, the amount of photons absorbed in the medium will be increased *a priori* when the medium becomes more and more opaque (the amount of photons transmitted being reduced); however, caution should be taken with such assessment as in the latter case, the mixing conditions can play a key role, all the more when other species are absorbing [32].

Fig. 6 illustrates the variation of the conversion of αT with [RB]. The experiments were conducted for two residence times while keeping constant the other operating conditions (V_R = 5 mL, $f \approx 1.7$, $q \approx 5$, $[\alpha T]_0 = 0.040\ mol\ L^{-1}$).

For each residence time τ, an optimal concentration of RB, noted $[RB]_{MAX}$, was reached, corresponding to a maximal conversion in αT.

From Fig. 6, two *scenari* can be described depending on the initial concentration of RB. Firstly, an increase of $[RB]_0$ until reaching $[RB]_{MAX}$ contributes to a strong increase of the conversion of αT. Secondly, for concentrations higher than $[RB]_{MAX}$, the conversion rate decreases slightly with $[RB]_0$. From this, two regimes can be defined.

- First regime: $[RB]_0 < [RB]_{MAX}$.

The local volumetric rate of photon absorption is directly proportional to $[RB]_0$ (Eq. (2)) and, therefore, the overall kinetic rate too (see Eq. (44)). Furthermore, the energy transfer from $^3RB^*$ to O_2 is a non-radiative transfer (see (Eq. (4)), also called Dexter mechanism. This process requires collisions between $^3RB^*$ and O_2. Consequently, if [RB] increases, then the frequency of such events (*i. e.* the energy transfer between $^3RB^*$ and O_2) will increase as well, and thus the production of $^1O_2$, leading to a rise of the conversion rate.

- Second regime: $[RB]_0 > [RB]_{MAX}$.

The conversion of αT decreases slightly with $[RB]_0$. Notably, the initial concentrations of RB used in these experiments are lower than the solubility of RB in EtOH, which is equal to $5.9 \times 10^{-2}\ mol\ L^{-1}$ (Gurr, 1971). This should prevent any aggregation of RB in the reaction medium, which could induce light scattering phenomena [48] Moreover, the emitted photon flux ($q_e = 1.7 \times 10^{-5}\ mol\ s^{-1}$) is 500 times higher than the maximum molar flow rate of RB ($F_{RB,MAX} = 3.0 \times 10^{-8}\ mol\ s^{-1}$). Therefore, if considering that only 1% of q_e is received in the reaction media in the extreme case, then photons will still be available in excess. As a consequence, the decrease of $\chi_{\alpha T}$ is not linked to "chemical limitations". This can be explained according to the light regime in the reactor.

For that, the characteristic light penetration distance, noted d_{pen}, was calculated in order to get an estimation of the light penetration into the reaction volume. Assuming a cartesian geometry and collimated rays (which does not represent the geometrical complexity of the present photochemical technology *a priori*), it can be equal to

$$d_{pen} = \frac{1}{\bar{\kappa}_{RB}.\ [RB]_0} \tag{45}$$

Eq. (45) involves the naperian molar absorption coefficient of RB, noted $\bar{\kappa}_{RB}$. In the case of a polychromatic light source, several methods can be used to approximate this parameter. One method describes the polychromatic light source as a monochromatic light source. Here, the employed light source being an assembly of four LEDs of 530 nm and two LEDs of 580 nm, one can assume it can be a monochromatic LED emitting at 547 nm (weighted average of both wavelengths). Considering that all the LEDs have the same photonic yield, it gives a first definition of $\bar{\kappa}_{RB} = \bar{\kappa}_a$ (Eq. (46)) [method a]

$$\bar{\kappa}_a = \kappa^{RB}_{547} = 1.3 \times 10^4\ m^2.\ mol^{-1} \tag{46}$$

The second method, which is clearly the more relevant way of calculation, consists of calculating an average naperian molar absorption coefficient over the spectral domain of the light sources by taking into account the light emission spectrum (see Fig. 3) [51,52]. It gives a second definition of $\bar{\kappa}_{RB} = \bar{\kappa}_b$ (Eq. (47)) [method b] where f^{LED}_λ is the density function of the light source at each wavelength λ (Fig. 3).

$$\bar{\kappa}_b = \frac{\int_{450}^{650} \kappa^{RB}_\lambda .\ f^{LED}_\lambda d\lambda}{\int_{450}^{650} f^{LED}_\lambda d\lambda} = 6.8 \times 10^3\ m^2.\ mol^{-1} \tag{47}$$

Once this naperian molar absorption coefficient is determined, d_{pen} can be derived as well as the dimensionless number d° defined as the ratio between d_{pen} and the diameter of the channel d_c. d° ≥ 1 corresponds to a reaction medium that is optically transparent (small optical thickness), a part of the light is lost by transmission through the back optical walls if the latter is transparent (no reflector) or opaque.

As showed in Fig. 6 for the residence time τ_{27}, $[RB]_{MAX,27} = 13 \times 10^{-5}\ mol\ L^{-1}$ corresponds to a dimensionless penetration distance d°_{27} equal to 0.7 (average value between the two methods). This value can be considered as close to unity when taking into account the approximations made to calculate $\bar{\kappa}$. Thus, under this condition, all the reaction media is almost entirely irradiated, no light-limitation occurs, explaining the high conversion level. When $[RB]_0$ increases, d_{pen} decreases (Eq. (45)): the medium becomes then more and more opaque, leading to a decrease of the fraction of irradiated volume where the photochemical reaction can take place in. As a consequence, dark zones appear in the reaction media (d° < < 1) (see

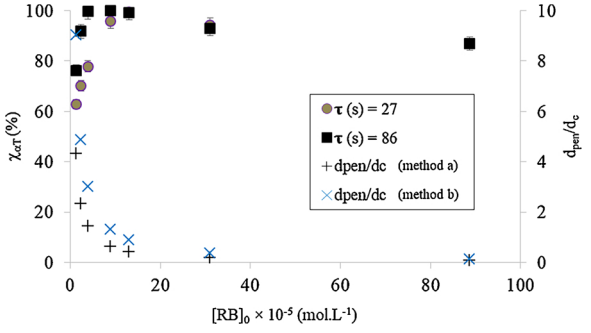

Fig. 6. Variation of the conversion of αT (%) and the dimensionless light distance penetration d° = d_{pen}/d_c (−) with the initial concentration of RB (mol L^{-1}) for two residence times τ (s) {$[\alpha T]_0 = 0.040\ mol\ L^{-1}$, V_R = 5 mL, f ≈ 1.7, q ≈ 5}. d_c is the diameter of the tube (= 1.3 mm).

Fig. 6). Then, the molecules located inside these dark zones do not interact efficiently with photons and the conversion decreases. Note that, for this residence time, the conversion rate is not affected by the photobleaching of RB since its rate was below 5% for these operating conditions (see Fig. 5). In the extreme case, when a stronger absorbing media is present, the irradiated volume is located in a narrow zone close to the optical wall, leading to a "surface reaction" or "film reaction" regime. In such a light-limited configuration (*i.e.* $[RB]_0 > > [RB]_{MAX}$), $d_{pen} \approx \delta$, with δ being the film thickness, commonly in the order of 50 µm [65], which lead to $d^\circ \approx 0.04$. Therefore, the role of the mixing along the light penetration length is crucial to efficiently renew the optical surface [32]. According to Fig. 6, the last point ($[RB]_0 = 8.9 \times 10^{-5}$ mol L^{-1}) would be close to such "film reaction" regime as $d^\circ \approx 0.06$. Remarkably, the conversion is still high (87%). Two explanations can be proposed: (1) the mixing and the gas-liquid mass transfer is so intense in Taylor flows that the medium contained in the liquid slugs can be efficiently transported in the irradiated film zone located close to the optical wall, and/or (2) most of the reaction occurs in the liquid films between the bubbles and the walls. By describing the reaction system as a unit cell (see Fig. 4), for $q \approx 5$ and a cylindrical shape for bubbles and liquid slugs, one can show that the volume of the liquid film V_{film} and the volume of the liquid slug V_{LS} are approximately the same (see Supplementary material, Section 6). This would confirm the first assumption.

The experiment was repeated with a longer residence time τ_{86} (see Fig. 6). The same trends were noticed, which confirms the reproducibility of the results obtained at a lower residence time. Besides, it was found that $[RB]_{MAX}$ is almost identical for both residence times. This result is logical in so far as this is mainly controlled by the irradiance field inside the reaction volume, which depends on the medium absorbing properties and on the incident photon density flux. With all other parameters being constant (in particular, q, f and V_R), increasing the residence time induces smaller total flow rates, and thus velocities of both phases. The fact that the value of $[RB]_{MAX}$ is not sensitive to this change in hydrodynamic conditions seems to confirm that the process is "light-limited".

This section showed that the obtained conversions of αT, when varying [RB], are the result of interactions between the irradiance field inside the reaction medium, the concentration field and the mixing profile. This latter result is clearly supported by Eq. (44); the reaction rate r depends on e^a_{RB} (expressed as a function of the concentration of RB and the irradiance field) and on the hydrodynamic behaviour (axial diffusion, radial diffusion and convection).

4.4. Effect of the mixing in the liquid slugs

To better investigate the coupling between the hydrodynamic conditions and the reaction rate, specific experiments were carried out using different reactor volumes. Following this approach, it is possible to obtain the same residence time under different hydrodynamic conditions as shown in Fig. 7. For example, to set τ equal to 0.66 min in a reactor volume of $V_{R1} = 5$ mL, the total volumetric flow rate Q_{T1} was set at 7.6 mL min^{-1}, whereas for a reactor volume $V_{R2} = 2$ mL, Q_{T2} was set at 3.3 mL min^{-1}. As $Q_{T1} > Q_{T2}$, the velocities of both phases (in particular the intensity of recirculation loops in the liquid slugs, see Fig. 7) will be higher when using V_{R1} than V_{R2}, and will also enhance the gas-liquid mass transfer (by increasing the rate of renewal of the bubble interface by the liquid). In all these experiments, the volume ratio q is kept constant to decouple the effect of the variation of bubble/liquid slug lengths from the conversion rate. The initial concentrations of RB and αT were equal to 4.0×10^{-5} mol L^{-1} and 0.037 mol L^{-1}, respectively.

Fig. 7 clearly demonstrates that, independent of the residence times, the conversion levels are always higher when using the largest reactor volume ($V_{R1} = 5$ mL), that is to say when improving the hydrodynamics conditions. In contrast, the photobleaching levels are lower in V_{R1} as shown in Fig. 8. These two results highlight (a) the beneficial correlation between the increase of the input volume flow rate and the mass transport properties and (b) the dependence of the photooxygenation performances on the hydrodynamic conditions.

Abiev [53] has demonstratedfor such reactors how the hydrodynamic regimemainly depends on the Capillary's number $\left(Ca = \frac{\mu . U_b}{\sigma}\right)$, where µ (Pa.s) is the viscosity of the liquid phase (here ethanol), σ (N m^{-1}) the surface tension and U_b (m s^{-1}) the velocity of the bubble. Below a critical value of Ca, noted Ca^* (= 0.7), for a horizontal tube, the flow is characterised by two symmetric recirculation vortices as illustrated in Fig. 9, named circulation mode. Under the present operating conditions, the values of Ca are lower than 9×10^{-3}, and the flow is then in a circulation mode.

Yang et al. [56] have also shown that the mass transport in the liquid slug can be divided into two phenomena within the circulation mode; the convection along the axial length of the tube and the diffusion along the radial length of the tube. Therefore, the rate of mass transport in the liquid slug K_{LS} can be approximated as follows:

$$K_{LS} = \frac{1}{\tau_{diff}} + \frac{1}{\tau_{conv}} \tag{48}$$

The characteristic time of convection τ_{conv} and of radial diffusion τ_{diff} can be estimated as follows:

$$\tau_{conv} = \frac{2.L_S}{U_L} \approx \frac{2.L_S.\ \pi.\left(\frac{d_c}{2}\right)^2}{Q_L} \tag{49}$$

$$\tau_{diff} = \frac{\left(\frac{d_c}{4}\right)^2}{D} \tag{50}$$

Where L_S is the length of the liquid slug, U_L the velocity of the liquid slug and D the diffusion coefficient of the transport species.

The operating conditions screened clearly favour the mixing by convection ($K_{LS} \approx 1/\tau_{conv}$) since $\tau_{diff} > 100.\tau_{Conv}$ for all experiments (see Supplementary material, Section 7).

In addition, from Eq. (49), it can be seen that Q_L is a critical parameter to favour the mixing by convection. Its increase leads to a rise of the mixing intensity within the liquid slug. Therefore, it is evident that $K_{LS1} > K_{LS2}$ which means a more intense circulation of liquid when using the reactor volume V_{R1} compared to V_{R2}. Such intensification in the mixing has several consequences when conducting the photooxygenation. In particular, if the frequency of contact by circulation between the gas and liquid increases, it enables to enhance the *third* and *fourth steps* describing the formation of $^1O_2$ and the formation of ascaridole, respectively; then the amount of dissolved O_2 and the value of ϕ_{O2} (Eq. (43)) will increase. Hence, the photoexcited species $^3RB^*$ has more probabilities to react with O_2 to generate $^1O_2$ than to be deactivated. The results illustrated in Fig. 8 are clearly in accordance with the model expressed by Eq. (44); the photobleaching level is indeed more

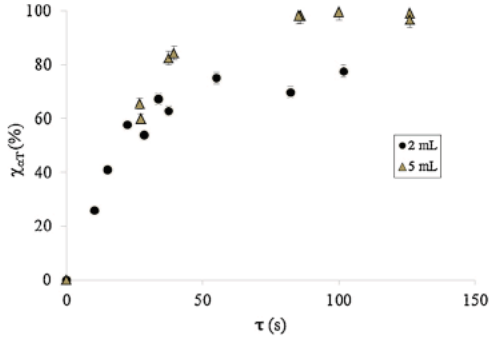

Fig. 7. Variation of the conversion of αT (%) with the residence time τ (s) for two different reactor volumes ($V_{R1} = 5$ mL and $V_{R2} = 2$ mL) and for fixed $q \approx 5$ and $f \approx 1.5$. $[\alpha T]_0 = 0.037$ mol L^{-1} and $[RB]_0 = 4.0 \times 10^{-5}$ mol L^{-1}.

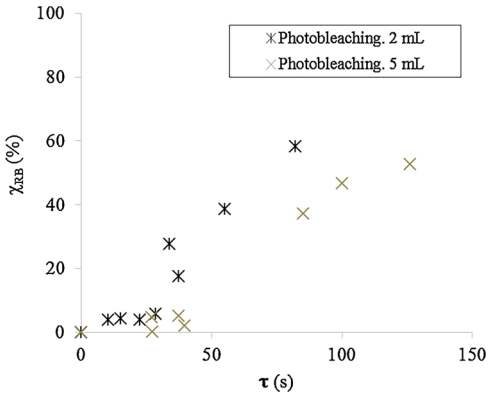

Fig. 8. Variation of the photobleaching rate χ_{RB} (%) with the residence time τ (s) for two different reactor volumes (V_{R1} = 5 mL and V_{R2} = 2 mL) and for fixed q ≈ 5 and f ≈ 1.5. $[RB]_0 = 4.0 \times 10^{-5}$ mol L^{-1} and $[\alpha T]_0 = 0.037$ mol L^{-1}.

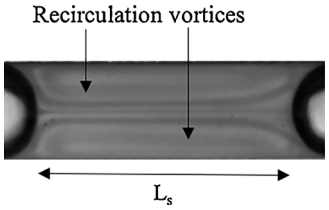

Fig. 9. Illustration of the two symmetric recirculation vortices in the liquid slug. Extracted from [58].

favoured for V_{R1} (*i. e.* $\chi_{RB}|_{V_{R1}} < \chi_{RB}|_{V_{R2}}$) meaning that $\varphi_{O_2}|_{V_{R1}} > \varphi_{O_2}|_{V_{R2}}$, which implies that $r|_{V_1} > r|_{V_2}$: the production of Asc is favoured in the case of higher volume flow rates (see the Fig. 7).

4.5. Effect of the stoichiometric proportion at the reactor's inlet

It is worth to highlight that high conversions (≈ 99%) within a residence time close to a minute were obtained in the case of an excess of O_2 ($f > 1$) (see Fig. 7). The variation of f is made experimentally possible by varying only the molar quantity of O_2 in the gas phase. According to Fig. 4, the decrease of q allows to reduce the bubble length while the liquid slug length remains almost unchanged in the present conditions. Two conclusions can be deduced for a given τ and V_R: (1) the velocity field in the liquid slug can be considered almost similar in both cases ($q = 5$ and $q = 3$) since L_S is approximately the same and (2) the molar quantity of O_2 decreases and those of α-terpinene and RB remain constant when decreasing q from 5 to 3. Thus, by decreasing q, the concentration of RB and αT (equal to 4.0×10^{-5} mol L^{-1} and 0.037 mol L^{-1}, respectively) and the mixing efficiency remain unchanged whereas the molar ratio between O_2 and α-terpinene, *i. e.* the parameter f, can be changed. This enables to study the influence of the mixing when $f \approx 1$ ($q \approx 3$) and to compare it to the one when $f \approx 1.5$ ($q \approx 5$).

When the stoichiometric proportion was established ($f \approx 1$) at the inlet of the reactor (see Fig. 10, the maximal conversion for V_{R1} and V_{R2} were 85% and 67%, respectively, whereas with $f > 1$, they were 99% and 75% (Fig. 7). In addition, the photobleaching phenomenon was more pronounced when $f \approx 1$, which can prevent the photoreaction from completing (Fig. 10 *versus* Fig. 8). Indeed, $\chi_{RB}\,|_{f>1}$ never exceeds the conversion level. Therefore, the conversion rates are higher and the photobleaching pathway limited with an excess of O_2. These results agree with the expression of the kinetic law. Indeed, according to the model (Eq. (44)), for the same hydrodynamic conditions and a given reaction volume, $\varphi_{O_2}|_{f>1} > \varphi_{O_2}|_{f=1}$ leads to the following inequality; $r|_{f>1} > r|_{f=1}$.

These two experiments ($f > 1$ and $f \approx 1$) demonstrated the need to monitor the gas-liquid hydrodynamics and to work with an excess of O_2 at the inlet of the reactor in order to efficiently achieve complete conversion to ascaridole.

4.6. Case of pure oxygen

As shown by Eq. (43), the dimensionless number ϕ_{O2} increases with the concentration of dissolved oxygen. Therefore, some final experiments were conducted using pure O_2 to enhance the kinetic of the photooxygenation, and thus to limit the photobleaching pathway.

The stoichiometric parameter f was set to 1.4 (excess of O_2) and the parameter q to 5; it resulted in an initial concentration of α-terpinene equal to 0.15 mol L^{-1}. The initial concentration of RB was set at 6.3×10^{-5} mol L^{-1}. The STY corresponding to {τ = 127 s; $\chi_{\alpha T}$ = 99%}, noted STY_{O2}, is equal to 1.2×10^{-3} mol s^{-1} L^{-1} (or 165 mg s^{-1} L^{-1}). This latter is 2.8 times higher than STY_{AIR} ($= 4.3 \times 10^{-3}$ mol s^{-1} L^{-1}). In addition, as shown in Fig. 11, the photobleaching pathway is considerably limited ($\chi_{RB} < 3\%$) when using pure O_2. As a consequence, it is clear that $\phi_{O2} >> 1$, which leads to simplify the expression of the kinetic law as follows;

$$r = e^{a}_{RB}.\ \phi^{O_2}.\ (\phi^{1}_{O_2 \rightarrow Asc}) \tag{51}$$

With

$$\phi^{O_2} = \left(\phi^{1}_{RB^* \rightarrow {}^3RB^*}\right).\left(\phi^{0}_{{}^3RB^* \rightarrow {}^1O_2}\right) = \left(\phi^{1}_{RB^* \rightarrow {}^3RB^*}\right).\left(\frac{k_{ET}.\,[O_2]}{k^{^3RB}_{Ph} + k^{^3RB}_{IC} + k^{^3RB}_{EtOH}.\,[EtOH] + k_{ET}.\,[O_2]}\right) \tag{52}$$

Where, $\phi^{0}_{RB^{3*} \rightarrow {}^1O_2}$ is the efficiency of $^1O_2$ formation from $^3RB^*$ without the quenching by α-terpinene ($k^{RB^3}_{Q} = 0$) and ϕ^{O_2} the quantum yield introduced in the Section 2.1 equal to 0.75.

4.7. Basic modelling

These experimental results were subsequently compared with the ones that would be predicted by basic modelling. For this, it is assumed that the flow reactor behaves as a plug flow reactor and that, when using pure oxygen, the limitation by the gas-liquid mass transfer becomes negligible. The following mass balance on the liquid phase can then be written for a given residence time (*i. e.* at a given axial position in the tube constituting the flow reactor) in which the variation of the concentration of α-terpinene with residence time is equal to the overall consumption rate of α-terpinene described by the kinetic law defined in Eq. (16).

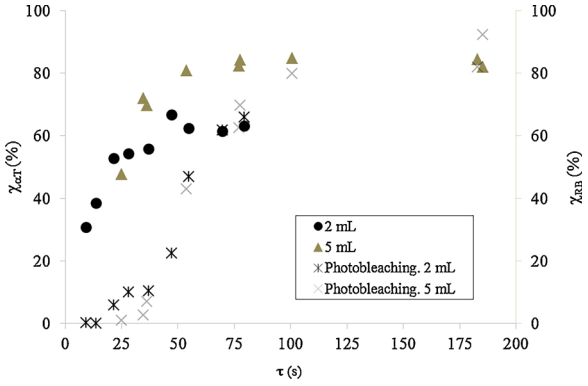

Fig. 10. Variation of the conversion rate of αT (%) and of the photobleaching rate (%) with the residence time τ (s) for two different reaction volumes (V_{R1} = 5 mL and V_{R2} = 2 mL) and for fixed q ≈ 5 and f ≈ 1 (stoichiometric condition). $[\alpha T]_0 = 0.037$ mol L^{-1} and $[RB]_0 = 4.0 \times 10^{-5}$ mol L^{-1}.

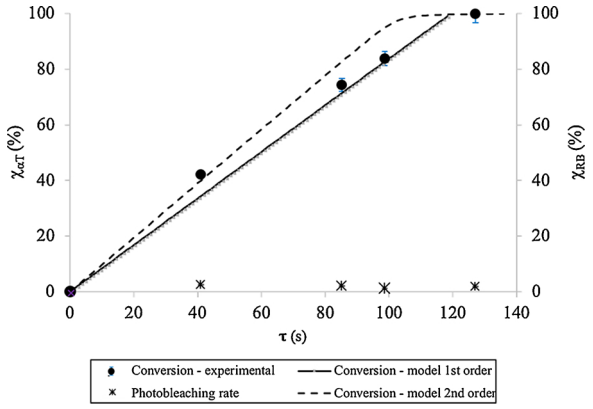

Fig. 11. Variation of the conversion of α-terpinene (%) with the residence time τ (s) with the use of pure O_2. q ≈ 5 and f ≈ 1.4. $[\alpha T]_0 = 0.15\,mol\,L^{-1}$ and $[RB]_0 = 6.3 \times 10^{-5}\,mol\,L^{-1}$. $V_R = 5\,mL$.

$$-\frac{d[\alpha T]}{d\tau} = [\alpha T]_0 . \frac{d\chi_{\alpha T}}{d\tau} = r = e^a_{RB} . \phi^{O_2} . (\phi^{1}{}_{O_2 \rightarrow Asc}) \quad (53)$$

We now assume that the light is monochromatic, emitted perpendicularly to the flow direction as a mono-directional and collimated light source, uniformly distributed along the reactor walls, and that the optical surface of the reactor is straight and non-reflective. It is important to note that these assumptions permitted a strategy of basic modelling and are to be verified in the present experimental set-up. In this case, the mean volumetric rate absorption of a photon by RB (averaged over a cross-sectional area of the tube) can be expressed as [30–32];

$$<e^a_{RB}> = \frac{q_p}{V_L} . (1 - \exp[-\bar{\kappa}_{RB} . [RB]_0 . d_c]) \quad (54)$$

Where q_P ($mol.s^{-1}$) is the incident photon flux, corresponding to the photon flux actually received in the reactor and V_L is the liquid volume defined as

$$V_L = (1 - \varepsilon_G) . V_R \quad (55)$$

With ε_G (-) the gas retention that can be approximated to $Q_G/(Q_G + Q_L)$. In the considered experimental conditions (Fig. 11), it was equal to 0.82.

Two cases can be distinguished, depending on the value of the order γ on the α-terpinene involved in Eq. (5) (reaction between $^1O_2$ and α-terpinene).

For an apparent order γ = 1, the following analytical expression of the irradiation time τ_i (= τ) with the conversion, $\chi_{\alpha T}$, can be established from Eqs. (27),(29),(53) and (54);

$$\tau_i = \frac{1}{q_p} . \frac{[\alpha T]_0 . V_L}{(1 - \exp[-\bar{\kappa}_{RB} . [RB]_0 . d_c]) . \phi^{O_2}} . \left(\chi_{\alpha T} + \frac{k_d}{k_R . [\alpha T]_0} . \ln\left(\frac{1}{1 - \chi_{\alpha T}}\right)\right) \quad (56)$$

For an apparent order γ > 1, the following expression can be obtained;

$$\tau_i = \frac{1}{q_p} . \frac{[\alpha T]_0 . V_L}{(1 - \exp[-\bar{\kappa}_{RB} . [RB]_0 . d_c]) . \phi^{O_2}} . \left(\chi_{\alpha T} + \frac{k_d}{k_R . [\alpha T]_0^{\gamma}} . \left(\frac{1}{(\gamma-1)(1 - \chi_{\alpha T})^{\gamma-1}} - \frac{1}{(\gamma-1)}\right)\right) \quad (57)$$

The results predicted by Eq. (56) (1st order) or Eq. (57) (2nd order) are reported in Fig. 11. For that, the ratio $\frac{k_d}{k_R [\alpha T]_0^{\gamma}}$ was reasonably chosen to be equal to 10^{-3} (*i. e.* the reaction rate is much higher than the deactivation of $^1O_2$). It is important to note that the sole fitting parameter is the incident photon flux q_P, which is determined *via* the method of least squares. Depending on the order γ (1st or 2nd) and on the method of calculation of $\bar{\kappa}$ (see Section 4.2) different values of q_p can be obtained as shown in Table 3.

Table 3
Incident photon flux inside the reaction media q_p deduced from the fitting between experimental conversion and the ones predicted by Eqs. (56) and (57), depending on the order γ and on the method chosen to estimate $\bar{\kappa}_{RB}$.

q_p ($mol\,s^{-1}$)	γ = 1	γ = 2
κ_a ($m^2\,mol^{-1}$)	3.0×10^{-6}	3.8×10^{-6}
$\bar{\kappa}_b$ ($m^2\,mol^{-1}$)	5.2×10^{-6}	6.6×10^{-6}

The values of q_p [$\bar{\kappa}_a$, γ = 1], q_p[$\bar{\kappa}_b$, γ = 1], q_p[$\bar{\kappa}_a$, γ = 2] and q_p[$\bar{\kappa}_b$, γ = 2] represent 18%, 31%, 22%, 39%, respectively, of the emitted photon flux, q_e (= $1.7 \times 10^{-5}\,mol\,s^{-1}$). Therefore, they are physically acceptable as these incident photon fluxes are smaller than the emitted photon flux ($q_p < q_e$) and the experimental set-up is not optimized in terms of energetic efficiency. The proposed models are then able to describe the global experimental trends, even if the assumptions made are very rough. And according to Fig. 11, the most representative model is the one corresponding to γ = 1 (1st order). Nevertheless, these basic models need to be improved in the future, in particular to take into account the non-collimated nature of the incident light and the cylindrical geometry of the microreactor tube. For this purpose, further experiments will also be required to determine rigorously the exact value of q_p, by means of chemical actinometry in the visible domain of light.

To conclude, it is interesting to discuss the consequences of the results obtained in terms of reaction monitoring. Regarding the experiments carried out in the Vapourtec® photoreactor, two operating domains can be clearly depicted; (a) photooxygenation with air, (b) photooxygenation with pure O_2.

(a) When air is used as a source of O_2, the first action is to determine the operating conditions that limit the photobleaching pathway (excess of O_2 and fast mixing), then the production of ascaridole should be conducted with [RB] ≈ $[RB]_{MAX}$ corresponding to d° ≈ 1 to maximize the conversion. With these specifications {τ = 27 s; time of run = 4 h; $[\alpha T]_0 = 0.037\,mol\,L^{-1}$}, a selective (> 98%) production of ascaridole has been successfully implemented in the photoreactor, leading to an optimal production of ascaridole equal to $3.3\,g\,h^{-1}$.
(b) The use of pure O_2 clearly avoids the photobleaching of RB and allows to simplify the expression of the kinetic law (Eq. (44)). It enables also to increase the STY by a factor of 2.8.

In the latter case, the characteristic time of the photooxygenation reaction, noted τ_R, can be defined as follows;

$$\tau_R = \frac{[\alpha T]_0}{<r>_{\chi_{\alpha T}=0}} = \frac{[\alpha T]_0}{<e^a_{RB}>_{\chi_{\alpha T}=0} . \phi^{O_2} \left(1 + \frac{k_d}{k_R [\alpha T]_0}\right)} \approx \frac{[\alpha T]_0}{<e^a_{RB}>_{\chi_{\alpha T}=0} . \phi^{O_2}} \quad (58)$$

With

$$<e^a_{RB}>_{\chi_{\alpha T}=0} = <e^a_{RB}> \quad (59)$$

Under these operating conditions, τ_R is found close to 120 s. It corresponds to a residence time where the conversion rate is equal to 99% (see Fig. 11). This highlights the relevance of the definition of τ_R (Eq. (58)) when pure O_2 is used. Finally, the Damköhler I (Da_I) number can then be properly defined;

$$Da_I = \frac{\tau_i}{\tau_R} \approx \chi_{\alpha T} + \frac{k_d}{k_R [\alpha T]_0} . \ln\left(\frac{1}{1 - \chi_{\alpha T}}\right) \quad (60)$$

Eq. (60) can be used to estimate the initial concentration of αT to choose to achieve a given conversion level.

5. Conclusions

This paper aimed at investigating a two-phase photochemical reaction (*i. e.* a sensitized photooxygenation) in an advanced LED-driven flow reactor module (Vapourtec® easy-photochem E-series), both from an experimental and modelling point of view. More particularly, the objective was to formalize the effects of the operating conditions (hydrodynamic conditions, initial concentration of reagents *etc.*) on the reaction performances. A photochemical engineering framework was proposed for this purpose, a methodology being rarely encountered in the present literature dealing with flow photochemistry. The photooxygenation of α-terpinene was chosen as a benchmark reaction, with ethanol as a green solvent and rose Bengal as a cheap photosensitizer of industrial interest.

For the first time, a specific effort was made to rigorously establish the kinetic law based on all reaction pathways, the latter being then used as a mean to provide an experimental strategy to identify the key operating parameters. Subsequently, the experiments carried out under continuous-flow conditions demonstrated that an operating domain (concentrations, flow rates) can be identified that allowed a quantitative and selective conversion into ascaridole while the photobleaching was operating moderately. It provided an important and promising result from an industrial perspective: to implement sensitized photooxygenations in a green solvent (ethanol) and with a low-cost photosensitizer (RB) within continuous-flow microstructured equipment at meso-scale. Indeed, the photobleaching of RB is not an issue anymore as operating conditions enabling its control can be identified.

By conducting other specific experiments to separate the effects of the different interconnected parameters, it was also shown that the hydrodynamic characteristics of the gas-liquid flow can have an effect on the conversion.

Finally, when pure oxygen was used, a first simplified model could be proposed to predict the conversion at the reactor's outlet. In the future, this simplified model needs to be improved, in particular by determining accurately the incident photon flux density using chemical actinometry in the visible domain and an advanced modelling of radiative transfer.

Acknowledgments

This work was financially supported by the Australian Research Council (ARC, DP130100794) and by the French Research Agency under its Collaborative Research Project program PICPOSS (ANR-15-CE07-0008-01). The authors thank Duncan Guthrie (Vapourtec Ltd, UK) for technical support.

Appendix A. Supplementary data

Supplementary data associated with this article can be found, in the online version, at https://doi.org/10.1016/j.cep.2018.05.015.

References

[1] P. Anastas, J. Warner, Green Chemistry: Theory and Practice, Oxford Univ. Press, New York, 1998 pp. 30.
[2] P. Anastas, J.B. Zimmerman, Through the 12 principles Green engineering, Environ. Sci. Technol. 37 (2003) 94A–101A.
[3] N. Hoffmann, Photochemical reactions as key steps in organic synthesis, Chem. Rev. 108 (2008) 1052–1103.
[4] T. Bach, J.P. Hehn, Synthetic methods photochemical reactions as key steps in natural product synthesis, Angew. Chem. Int. Ed. 50 (2011) 1000–1045.
[5] A.M. Braun, M.-T. Maurette, E. Oliveros, Photochemical Technology, Wiley, Chichester, United Kingdom, 1991.
[6] A. Albini, V. Dichiarate, The 'belle époque' of photochemistry, Photochem. Photobiol. Sci. 8 (2009) 248–254.
[7] N. Hoffmann, Efficient photochemical electron transfer sensitization of homogeneous organic reactions, J. Photochem. Photobiol. C Photochem. Rev. 9 (2008) 43–60.
[8] M.D. Kärkäs, J.A. Porco, C.R.J. Stephenson, Photochemical approaches to complex chemotypes: applications in natural product synthesis, Chem. Rev. 116 (2016) 9683–9747.
[9] A. Juzeniene, M. Grigalavicius, M. Juraleviciute, W.B. Grant, Phototherapy and vitamin D, Clin. Dermatol. 34 (2016) 548–555.
[10] V. Ramamurthy, B. Mondal, Supramolecular photochemistry concepts highlighted with select examples, J. Photochem. Photobiol. C Photochem. Rev. 23 (2015) 68–102.
[11] K. Watanabe, D. Menzel, N. Nilius, H. Freund, Photochemistry on metal nanoparticles, Chem. Rev. 106 (2006) 4301–4320.
[12] M.C. Derosa, R.J. Crutchley, Photosensitized singlet oxygen and its applications, Coord. Chem. Rev. 234 (2002) p. 351.
[13] A.A. Ghogare, A. Greer, Using singlet oxygen to synthesize natural products and drugs, Chem. Rev. 116 (2016) 9994–10034.
[14] A.A. Krasnovsky, Early history of spectroscopic and photochemical studies with contributions of A.N. Terenin and Terenin's school, J. Photochem. Photobiol. A Chem. 354 (2018) 11–24.
[15] S. Meyer, D. Tietze, S. Rau, B. Sch, Photosensitized oxidation of citronellol in microreactors, J. Photochem. Photobiol. A Chem. 186 (2007) 248–253.
[16] O. Shvydkiv, C. Limburg, K. Nolan, M. Oelgemöller, Synthesis of juglone (5-hydroxy-1,4-naphthoquinone) in a falling film microreactor, J. Flow Chem. 2 (2012) 52–55.
[17] F. Lévesque, P.H. Seeberger, Continuous-flow synthesis of the anti-malaria drug artemisinin, Angew. Chem. Int. Ed. 51 (2012) 1706–1709.
[18] A. Yavorskyy, O. Shvydkiv, C. Limburg, K. Nolan, Y.M.C. Delauré, M. Oelgemöller, Photooxygenations in a bubble column reactor, Green Chem. 14 (2012) 888–892.
[19] D. Ziegenbalg, D. Kralisch, OLEDs as prospective light sources for microstructured photoreactors, Photochem. Photobiol. Sci. 13 (2014) 1005–1015.
[20] Y. Nagasawa, K. Tanba, N. Tada, E. Yamaguchi, A. Itoh, A study of aerobic photooxidation with a continuous-flow microreactor, Synlett 26 (2015) 412–415.
[21] K. Mizuno, Y. Nishiyama, T. Ogaki, K. Terao, H. Ikeda, K. Kakiuchi, Utilization of microflow reactors to carry out synthetically useful organic photochemical reactions, J. Photochem. Photobiol. C Photochem. Rev. 29 (2016) 107–147.
[22] O. Shvydkiv, K. Jähnisch, N. Steinfeldt, A. Yavorskyy, M. Oelgemöller, Visible-light photooxygenation of α-terpinene in a falling film microreactor, Catal. Today 308 (2018) 102–118.
[23] C. Mendoza, M. Winter, C.R. Horn, A. Vizza, L. Dreesen, J.M. Monbaliu, Scalable photocatalytic oxidation of methionine under continuous- flow conditions, Org. Process Res. Dev. 21 (2017) 1435–1438.
[24] M. Oelgemöller, N. Hoffman, Studies in organic and physical photochemistry – an interdisciplinary approach, Org. Biomol. Chem. 14 (2016) 7392–7442.
[25] M. Pagliaro, Making APIs and fine chemicals with light, Chem. Today 35 (2017) 84–85.
[26] K.N. Loponov, J. Lopes, M. Barlog, E.V. Astrova, A.V. Malkov, A.A. Lapkin, Optimization of a scalable photochemical reactor for reactions with singlet oxygen, Org. Process Res. Dev. 18 (2014) 1443–1454.
[27] D. Ziegenbalg, B. Wriedt, Investigation of photon fluxes within microstructured photoreactors revealing great optimization potentials, Chem. Eng. Technol. 39 (2016) 1–13.
[28] M.E. Leblebici, B. Van Den Bogaert, G.D. Stefanidis, T. Van Gerven, Efficiency vs. productivity in photoreactors, a case study on photochemical separation of Eu, Chem. Eng. J. 310 (2017) 240–248.
[29] T. Aillet, K. Loubière, O. Dechy-Cabaret, L. Prat, Accurate measurement of the photon flux received inside two continuous flow microphotoreactors by actinometry, Int. J. Chem. React. Eng. 12 (2014) 257–269.
[30] T. Aillet, K. Loubière, L. Prat, O. Dechy-Cabaret, Impact of the diffusion limitation in microphotoreactors, AIChE 61 (2015) 1284–1299.
[31] S. Elgue, T. Aillet, K. Loubière, A. Conté, O. Dechy-Cabaret, L. Prat, C.R. Horn, O. Lobet, S. Vallon, Flow photochemistry: a meso-scale reactor for industrial applications, Chem. Todays 33 (2015) 42–44.
[32] K. Loubière, M. Oelgemöller, T. Aillet, O. Dechy-Cabaret, L. Prat, Continuous-flow photochemistry: a need for chemical engineering, Chem. Eng. Process. Process Intensif. 104 (2016) 120–132.
[33] R.C.R. Wootton, R. Fortt, A.J. De Mello, A microfabricated nanoreactor for safe, continuous generation and use of singlet oxygen, Org. Process Res. Dev. 6 (2002) 2000–2002.
[34] T. Carofiglio, P. Donnola, M. Maggini, M. Rossetto, E. Rossi, Fullerene-promoted singlet-oxygen photochemical oxygenations in glass-polymer microstructured reactors, Adv. Synth. Catal. 350 (2008) 2815–2822.
[35] A.A. Lapkin, V.M. Boddu, G.N. Aliev, B. Goller, S. Polisski, D. Kovalev, Photo-oxidation by singlet oxygen generated on nanoporous silicon in a LED-powered reactor, Chem. Eng. J. 136 (2008) 331–336.
[36] J.F.B. Hall, X. Han, M. Poliakoff, R.A. Bourne, M.W. George, Maximising the efficiency of continuous photo-oxidation with singlet oxygen in supercritical CO2 by use of fluorous biphasic catalysis, Chem. Commun. 48 (2012) 3073–3075.
[37] K.S. Elvira, R.C.R. Wootton, N.M. Reis, M.R. Mackley, A.J. DeMello, Through-wall mass transport as a modality for safe generation of singlet oxygen in continuous flows, ACS Sustain. Chem. Eng. 1 (2013) 209–213.
[38] C.Y. Park, Y.J. Kim, H.J. Lim, J.H. Park, M.J. Kim, S.W. Seo, C.P. Park, Continuous flow photooxygenation of monoterpenes, RSC Adv. 5 (2015) 4233–4237.
[39] O. Dechy-Cabaret, F. Benoit-Vical, Preparation and antimalarial activities of 'Trioxaquines', new modular molecules with a trioxane skeleton linked to a 4-aminoquinoline, Chembiochem 218 (2000) 281–283.
[40] F. Ronzani, N. Costarramone, S. Blanc, A.K. Benabbou, M. Le Bechec, T. Pigot, M. Oelgemöller, S. Lacombe, Visible-light photosensitized oxidation of α-terpinene using novel silica-supported sensitizers: photooxygenation vs. photodehydrogenation, J. Catal. 303 (2013) 164–174.

[41] J.M. Tobin, T.J.D. McCabe, A.W. Prentice, S. Holzer, G.O. Lloyd, M.J. Paterson, V. Arrighi, P.A.G. Cormack, F. Vilela, Polymer-supported photosensitizers for oxidative organic transformations in flow and under visible light irradiation, ACS Catal. 7 (2017) 4602–4612.
[42] M. Oelgemöller, C. Jung, J. Mattay, Green photochemistry: production of fine chemicals with sunlight, Pure Appl. Chem. 79 (2007) 1939–1947.
[43] F. Wilkinson, W.P. Helman, A.B. Ross, Quantum yields for the photosensitized formation of the lowest electronically excited State of molecular oxygen in solution, J. Chem. Phys. Ref. Data 22 (1993) 113–262.
[44] F. Wilkinson, W.P. Helman, A.B. Ross, Rate constants for the decay and reactions of the lowest electronically excited singlet State of molecular oxygen in solution. An expanded and revised compilation, J. Chem. Phys. Ref. Data 24 (1995) 663–1021.
[45] C. Schweitzer, R. Schmidt, Physical mechanisms of generation and deactivation of singlet oxygen, Chem. Rev. 103 (2003) 1685–1757.
[46] C.R. Lambert, I.E. Kochevar, Electron transfer quenching of the rose bengal triplet state, Photochem. Photobiol. 66 (1997) 15–25.
[47] A. Zakrzewski, D.C. Neckers, Bleaching products of rose bengal under reducing conditions, Tetrahedron 43 (1987) 4507–4512.
[48] D.C. Neckers, Review: rose bengal, J. Photochem. Photobiol. A Chem. 47 (1989) 1–29.
[49] K.-H. Pfoertner, V. Oppenländer, Ullmann's encyclopedia of industrial chemistry, Photochemistry, Wiley-VCH Verlag, Weinheim, 2000.
[50] B.M. Monroe, Rate constants for the reaction of singlet oxygen with conjugated dienes, J. Am. Chem. Soc. 4 (1981) 1–4.
[51] V. Rochatte, G. Dahi, A. Eskandari, J. Dauchet, F. Gros, M. Roudet, J.F. Cornet, Radiative transfer approach using Monte Carlo method for actinometry in complex geometry and its application to Reinecke salt photodissociation within innovative pilot-scale photo(bio)reactors, Chem. Eng. J. 308 (2017) 940–953.
[52] J.F. Cornet, A. Marty, J.B. Gros, Revised technique for the determination of mean incident light fluxes on photobioreactors, Biotechnol. Prog. 13 (1997) 408–415.
[53] R.S. Abiev, Circulation and bypass modes of the slug flow of a gas – liquid mixture in Capillaries, Theor. Found. Chem. Eng. 43 (2009) 313–321.
[56] L. Yang, M.J. Nieves-remacha, K.F. Jensen, Simulations and analysis of multiphase transport and reaction in segmented flow microreactors, Chem. Eng. Sci. 169 (2017) 106–116.
[58] L. Yang, K. Loubière, N. Dietrich, C. Le, C. Gourdon, G. Hébrard, Local investigations on the gas-liquid mass transfer around Taylor bubbles flowing in a meandering millimetric square channel, Chem. Eng. Sci. 165 (2017) 192–203.
[59] R.S. Abiev, I.V. Lavretsov, Hydrodynamics of gas – liquid slug flow in capillaries: comparing theory and experiment, Theor. Found. Chem. Eng. 45 (2011) 251–263.
[60] R. Pohorecki, P. Sobieszuk, J. Aubin, Hydrodynamics and mass transfer in gas-liquid flows in microreactors, Chem. Eng. Technol. 35 (2012) 1346–1358.
[61] T. Bandara, N. Nguyen, G. Rosengarten, Slug flow heat transfer without phase change in microchannels: a review, Chem. Eng. Sci. 126 (2015) 283–295.
[62] S. Haase, D. Yu, T. Salmi, Review on hydrodynamics and mass transfer in minichannel wall reactors with gas – liquid Taylor flow, Chem. Eng. Res. Des. 113 (2016) 304–329.
[63] R.S. Abiev, Analysis of local pressure gradient inversion and form of bubbles in Taylor flow in microchannels, Chem. Eng. Sci. 174 (2017) 403–412.
[64] F. Lévesque, P.H. Seeberger, Highly efficient continuous flow reactions using singlet oxygen as a 'Green' reagent, Org. Lett. 13 (2011) 5008–5011.
[65] C. Butler, E. Cid, A. Billet, Chemical engineering research and design modelling of mass transfer in Taylor flow: investigation with the PLIF-I technique, Chem. Eng. Res. Des. 115 (2016) 292–302.